Lithos 314–315 (2018) 400–424

Contents lists available at ScienceDirect

Lithos

journal homepage: www.elsevier.com/locate/lithos

Polycyclic Palaeozoic evolution of accretionary orogenic wedge in the southern Chinese Altai: Evidence from structural relationships and U–Pb geochronology

Arnaud Broussolle [a], Carmen Aguilar [b], Min Sun [a,*], Karel Schulmann [b,c], Pavla Štípská [b,c], Yingde Jiang [d], Yang Yu [a,d], Wenjiao Xiao [e], Sheng Wang [d], Jitka Míková [f]

[a] Department of Earth Sciences, The University of Hong Kong, Pokfulam Road, Hong Kong, China
[b] Centre for Lithospheric Research, Czech Geological Survey, Klárov 3, 11821 Praha 1, Czech Republic
[c] Ecole et Observatoire des Sciences de la Terre, Institut de Physique du Globe de Strasbourg – CNRS UMR7516, Université de Strasbourg, F-67084 Strasbourg Cedex, France
[d] Key Laboratory of Isotope Geochronology and Geochemistry, Guangzhou Institute of Geochemistry, Chinese Academy of Sciences, 510640 Guangzhou, China
[e] State Key Laboratory of Lithospheric Evolution, Institute of Geology and Geophysics, Chinese Academy of Sciences, 100029 Beijing, China
[f] Czech Geological Survey, Geologická 6, 15200 Praha 5, Czech Republic

ARTICLE INFO

Article history:
Received 29 January 2018
Accepted 4 June 2018
Available online 8 June 2018

Keywords:
Chinese Altai
Devonian and Permian metamorphism
Structural synthesis
U–Pb zircon dating
Permian exhumation

ABSTRACT

Structural analysis and U–Pb geochronological study on zircons from the southern Chinese Altai (the Kalasu area, SE of the Altai city) show that the Cambro-Ordovician accretionary wedge (ca. 520–492 Ma) underwent four major geological events: 1) emplacement of Early Devonian magmas (ca. 410–400) associated with formation of a volcano-sedimentary cover, 2) major Middle Devonian (ca. 390–374 Ma) tectono-metamorphic event, 3) Late Devonian-Early Carboniferous folding without apparent metamorphism, and 4) a regional folding with localized Early Permian high- to ultrahigh-temperature reworking (ca. 300–280 Ma). The Early Devonian magmatism is characterized by emplacement of mafic rocks and granitoids in the centre of the NE-SW profile, coevally with granitoid magmatism and rhyolite volcanism in the southwest and northeast, respectively. The whole volcano-sedimentary and magmatic edifice was transposed by sub-horizontal metamorphic fabric associated with variable metamorphic degrees in different areas ranging from greenschist facies in the northeast (mu + bi±g) to amphibolite facies in the southwest (st + g ± sill) and granulite facies in the centre (g + sill+kfs). This metamorphic architecture, distribution of magmatism and character of metamorphic zircon populations allow to correlate these areas with upper, middle and lower orogenic crust that developed during important vertical shortening and horizontal flow in Middle Devonian. Subsequently, the whole edifice was affected by regional NE-SW trending upright (possibly Late Devonian-Early Carboniferous) folding. Finally, Early Permian shortening produced NW-SE trending regional upright folds in the southwest and northeast and a crustal-scale vertical, tabular deformation zone in the centre. The Permian deformation is accompanied by granulite facies (kfs + cd + sill+g) metamorphism and anatexis reworking the Devonian lower orogenic crust, with extensive resetting and growth of new zircons and with intrusions of Permian granites and gabbros. This study suggests that the Early Permian event was related to massive perturbation of thermal structure of the mantle lithosphere due to the collision of the Junggar arc with the Chinese Altai terrane.

1. Introduction

Collisional orogenic systems are usually characterized by early subduction-related high-pressure (*HP*) metamorphism and deformation, followed by high-temperature (*HT*) re-equilibration, crustal thickening and melting (Dewey et al., 1993). Some collisional orogens even record polycyclic orogenic evolution such as Alpine reworking of the Variscan orogen in southern Europe (e.g. Lardeaux and Spalla, 1991) and Caledonian reworking of the Proterozoic orogenic belt in Scandinavia (e.g. Austrheim, 1990). These repeated collisional cycles are of a characteristic feature of recurrent amalgamation of continental blocks associated with closure of small oceanic basins typical for the Pangaea plate system (Collins, 2003). In contrast, the accretionary orogens at the periphery of the Pacific Ocean are characterized by tectonic switching resulting in alternations of *HP*-*LT* and *LP*-*HT* metamorphic cycles, due to subduction-related compression alternating with lithospheric extension and associated melting of fertile sediments (Collins, 2002). This tectonic switching is interpreted to result from advancing and retreating modes of a single long lasting subduction of an oceanic plate and thus

* Corresponding author.
E-mail address: minsun@hku.hk (M. Sun).

https://doi.org/10.1016/j.lithos.2018.06.005
0024-4937/

can be regarded as an example of a monocyclic evolution (Beltrando et al., 2007). So far, tectono-thermal effects of a second orogenic cycle on an early accretionary system have not been reported and the possible polycyclic reworking thus represents a challenge in our understanding of behaviour of accreted oceanic material during its incorporation into continents.

The Central Asian Orogenic Belt (CAOB) represents an excellent and unique example of giant accretionary system that is affected by two orogenic cycles: a Devono-Carboniferous accretion of Cambrian to Early Devonian oceanic assemblages with Precambrian continental blocks, followed by an orthogonal Permo-Triassic shortening of the whole accreted system (Lehmann et al., 2010; Xiao et al., 2015). The tectono-thermal effects of both events are best developed in a giant 2500 km long volcano-sedimentary accretionary prism; i.e. the so called Altai Orogenic Belt (Jiang et al., 2016, 2017). The prism consists dominantly of Cambro-Ordovician greywacke turbidites covered by Silurian and Devonian passive margin sequences in China, Mongolia and Russia (Jiang et al., 2017; Kröner et al., 2010). The Early Palaeozoic sediments experienced important regional Barrovian metamorphism followed locally by migmatitization and formation of orthopyroxene-bearing granulites in deep crustal levels Burenjargal et al., 2014, 2016; Jiang et al., 2010, 2015; Kozakov et al., 2002). This metamorphic event is characterized by massive melting of fertile sediments and is associated with intrusions of numerous arc-like granitoids at upper crustal levels, leaving a granulite residuum beneath the whole Chinese part of the Altai Orogenic Belt (Hanžl et al., 2016; Jahn et al., 2000; Jiang et al., 2016). A second and less extensive Permian metamorphic event was dated by monazite and zircon and is characterized by amphibolite- and granulite-facies rocks and by intrusions of granitoids, pegmatites and gabbros (Burenjargal et al., 2016; Nakano et al., 2015; Zhang et al., 2014; Zheng et al., 2007). In the Mongolian Altai, the Permian magmatic and metamorphic rocks are restricted to several E-W trending zones (Guy et al., 2014; Kovalenko et al., 2004; Yarmolyuk et al., 2013), while in the Chinese Altai, the Permian event affected mainly its southern part in a NW-SE trending zone parallel to the Erqis fault (Li et al., 2014; Tong et al., 2014a, 2014b; Zheng et al., 2007).

In addition, recent studies show that the whole Altai Orogenic Belt was affected by Devonian and Permian upright folding, which modified lateral distribution of metamorphosed middle and lower crustal rocks and unmetamorphosed sediments (Jiang et al., 2015; Li et al., 2015a, 2015b; Zhang et al., 2015). It is therefore important to decipher the real architecture of the lower, middle and upper crust, which resulted from the Middle Devonian subhorizontal crustal flow and the Late Devonian-Early Carboniferous upright folding and doming of the accretionary wedge (Broussolle et al., 2015; Jiang et al., 2015, 2016; Lehmann et al., 2017). After reconstruction of the post-Devonian metamorphic and lithological pattern it is possible to assess the influence and relative importance of the superimposed Permian metamorphism, folding and shearing. These two issues are in the core of the present study. A detailed geological and structural mapping of an area of ~37 × 33 km^2 in the southern part of the NW Chinese Altai is combined with U–Pb zircon geochronology of sedimentary, metamorphic and magmatic rocks, in order to identify protolith ages, timing of intrusions and partial melting events. By doing that we are able to discriminate geometries, extent and ages of main orogenic fabrics related to Palaeozoic magmatic, tectonic and metamorphic events. Finally, a new 3D crustal-scale model of the post-Permian crustal architecture of the southern part of the Altai Orogenic Belt is proposed, which has pivotal significance for the southern Central Asian Orogenic Belt.

2. Geological setting

2.1. Geology of the NW Chinese Altai

The NW-SE trending Altai Orogenic Belt extends for 2500 km from Russia and E Kazakhstan in the west, through NW China to SW Mongolia in the east (Fig. 1 inset; Jahn et al., 2000; Mossakovsky et al., 1993; Sengör et al., 1993; Windley et al., 2007; Xiao et al., 1992). The NW Chinese part of the Altai Orogenic Belt (here the Chinese Altai) represents a small segment of the giant Altai accretionary wedge (Chen and Jahn, 2002; Jiang et al., 2016). The Chinese Altai is mainly composed of variably metamorphosed Cambro-Ordovician to Carboniferous volcano-sedimentary sequence, including sandstone, siltstone, shale and minor limestone, intercalated with basaltic and rhyolitic lavas. The Chinese Altai can be divided into five NW-SE extending lithostratigraphic units interpreted as suspect fault bounded terranes which are considered to have distinct stratigraphy, metamorphism and deformation pattern (Fig. 1; e.g. He et al., 1990; Windley et al., 2002; Xiao et al., 2004). The North Altaishan terrane, located in the eastern part (terrane 1 in Fig. 1), is composed of Early Devonian and Late Carboniferous neritic clastic sediments and limestones intercalated with minor island arc volcanic rocks, that belong to the Altai and Kalaerqisi formations (Windley et al., 2002). The Northwest Altaishan terrane, occupying the northern part of Chinese Altai (terrane 2 in Fig. 1), comprises a 4–6 km thick Cambro-Ordovician turbiditic and pyroclastic sequence, known as the Habahe Formation (Cai et al., 2011a; Long et al., 2007, 2008). This terrane is also composed of the Dongxileke and Bahaiba formations, which represent a minor Devonian volcanic suite and a Cambro-Ordovician turbiditic sequence, respectively, and are similar to the Habahe Formation in lithology (Long et al., 2012). The Central Altai terrane, situated in the central to southeastern part of the Chinese Altai (terrane 3 in Fig. 1), is also composed of a Cambro-Ordovician to Silurian turbiditic and pyroclastic sequence, similar to the Habahe Formation, and are known in the central area as the Kulumiti Formation (Wang et al., 2014b). The Qiongkuer-Abagong and South Altaishan terranes are two NW-SE narrow belts in the southern Chinese Altai (terrane 4 & 5 in Fig. 1, respectively). The Qiongkuer-Abagong terrane is made up of Cambro-Ordovician sediments with Late Silurian to Early Devonian island arc-type lavas and pyroclastic rocks in its lower part (the Kangbutiebao Formation) and with Middle Devonian marine clastic sedimentary sequence in the upper part (the Altai Formation) (Cai et al., 2011a). The South Altaishan terrane is similar to the North Altaishan terrane, and contains metamorphic rocks (amphibolite-facies para- and orthogneiss), a sequence of Devonian fossiliferous sediments belonging to the Altai Formation, and a late Carboniferous volcano-clastic rocks refered as the Kalaerqisi Formation. The metavolcano-sedimentary sequences of the Chinese Altai are separated from the Junggar block in the south by one of the largest transcurrent faults in Central Asia, the NW-trending Erqis fault zone (Fig. 1; He et al., 1990; Windley et al., 2002). The 10-km wide Erqis fault zone contains fragments of Devonian ophiolitic rocks (Wang et al., 2003) and is considered to be the suture between the Junggar island arc system subducted beneath the Chinese Altai orogenic Belt during the Early to Middle Palaeozoic (Li et al., 2015a; Zhang et al., 2012).

All these metavolcano-sedimentary sequences were variably metamorphosed and deformed during Devonian and Permian tectono-thermal events, ranging from greenschist to upper amphibolite facies and locally reached granulite facies conditions with some migmatitization (Wei et al., 2007; Zhuang, 1994). Metamorphic grade related to the first tectono-metamorphic cycle increases from Early Devonian to Cambro-Ordovician rocks from chlorite-biotite, garnet, staurolite, kyanite, sillimanite and garnet-cordierite grade (Jiang et al., 2015; Zhuang, 1994). The first cycle, which is extensive in the whole Chinese Altai Belt, took place during Middle Devonian (ca. 390 Ma; Jiang et al., 2010) and was associated with two distinct metamorphic stages characterized by M1 Barrovian-type M*T*–M*P* and M2 Buchan-type H*T*–*LP* field gradients (He et al., 1990; Jiang et al., 2015; Wang et al., 2009b; Wei et al., 2007). The metamorphic conditions were recently estimated by mineral equilibria modelling in the Buerjin–Qiongkuer area (northwestern part of the Qiongkuer Abagong terrane; Jiang et al., 2015). For the M1 Barrovian-type metamorphism, the *P*–*T* conditions range from ~4–4.5 kbar and 550 °C to ~6 kbar and 600 °C. The M2 metamorphism

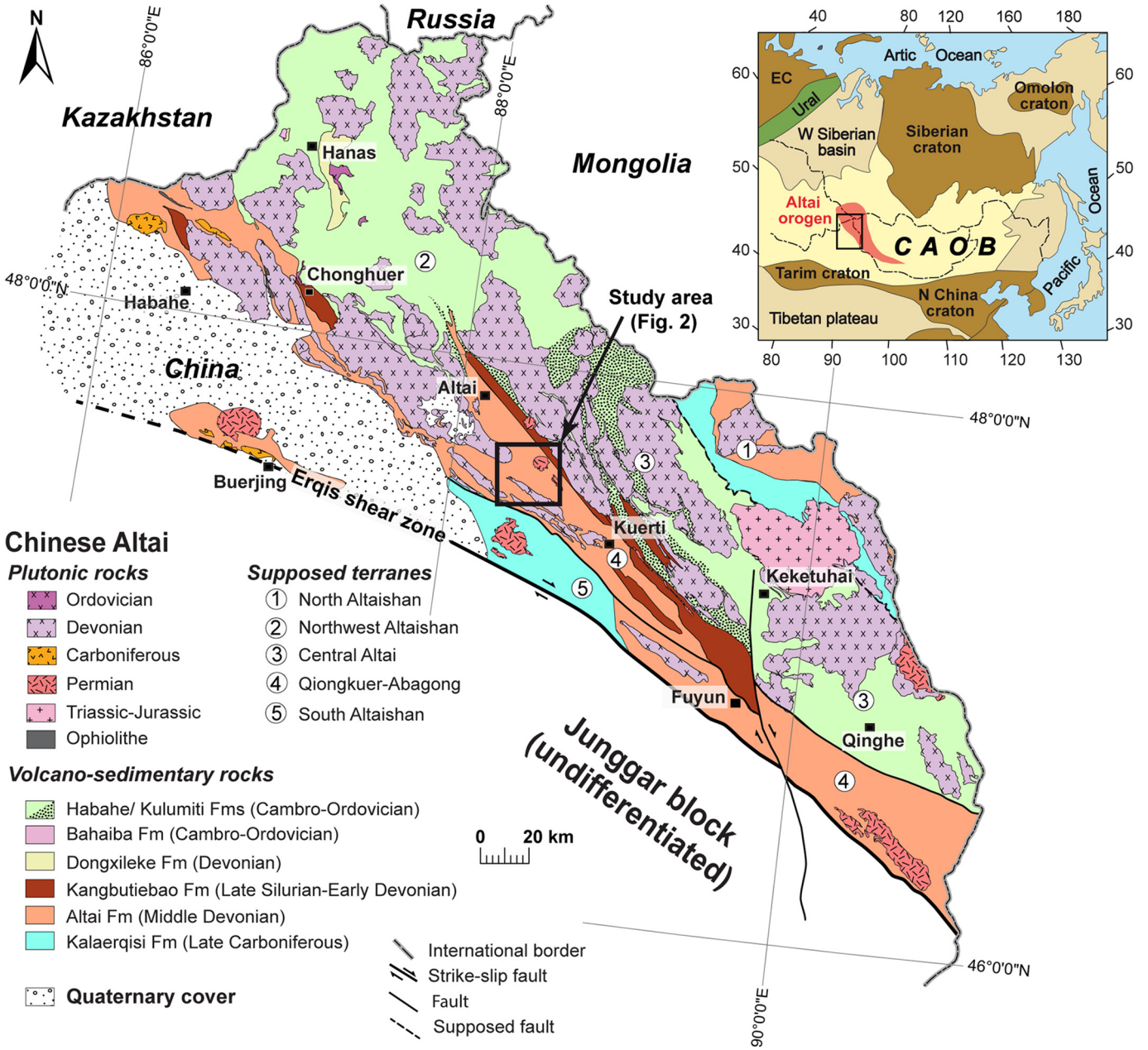

Fig. 1. Generalized geological map of the Chinese Altai showing the different supposed terranes and the main lithostratigraphical units (modified after Li et al., 2015b). The study area is outlined and shown in Fig. 2. The upper right inset shows the extension of the Central Asian Orogenic Belt (CAOB), the location of the Altai orogenic Belt (outlined by red shading) and the Chinese Altai orogen (delineated by small square) (modified after Jahn et al., 2000). EC: Eastern European craton.

is related to extensive anatexis marked by prograde evolution from ~6 kbar and 600 °C to ~8 kbar and 650 °C, followed by post-peak re-equilibration at ~5–6 kbar at 700–750 °C (Jiang et al., 2015). According to Jiang et al. (2015), the two metamorphic stages can be correlated with distinct phases of deformation: the Barrovian M1 developed within a sub-horizontal metamorphic S1 fabric, while the M2 anatexis was associated with a steep S2 foliation. The inferred clockwise *P–T–d* path suggests that the two tectono-metamorphic stages reflect a single geodynamic process characterized by a progressive burial history during the D1-M1 followed by a near-isothermal decompression during the D2-M2 stage. Associated with this Devonian tectono-metamorphic cycle, voluminous granitoids, forming nearly 40% of the map surface, were emplaced intermittently from ca. 460 to 370 Ma (Fig. 1; e.g. Briggs et al., 2007; Sun et al., 2008, 2009; Tong et al., 2007; Wang et al., 2006; Windley et al., 2002; Yuan et al., 2007). The geochemical data show that the Early Palaeozoic granitoids are mostly metaluminous or weakly peraluminous, calc-alkaline with typical syn-orogenic arc signature (Cai et al., 2011b; Wang et al., 2006).

The second tectono-metamorphic cycle is Early Permian (between ca. 290 to 260 Ma; Briggs et al., 2007; Chen et al., 2006; Hu et al., 2000; Wang et al., 2009b; Zheng et al., 2007), and is recognized only in a narrow NW-SE trending zone in the Qiongkuer-Abagong and South Altaishan terranes (Fig. 1; Li et al., 2014; Tong et al., 2013, 2014a; Wang et al., 2014a). It is characterized by anatexis and metamorphism reaching ultrahigh-temperature conditions (UHT; >900 °C), and is recognized mostly in metapelites with sillimanite, spinel, orthopyroxene and garnet-cordierite mineral assemblages (Li et al., 2004, 2010; Tong et al., 2013, 2014a; Wang et al., 2009b; Zhang et al., 2012). The Permian anatexis and up to UH*T* metamorphism took place coevally with an extensive Permian mafic to granitoid magmatism (ca.

280–260 Ma; Pirajno et al., 2008; Tong et al., 2014a; Zhang et al., 2010). This magmatism is attributed to a post-orogenic or anorogenic extensional setting in the Altai region (Briggs et al., 2007; Chen and Han, 2006; Han et al., 2004; Tong et al., 2006, 2014a; Zhang et al., 2012). In addition, a large number of post-collision Permian to Jurassic pegmatites were emplaced in the Chinese Altai (between ca. 260 to 191 Ma; Chen, 2011; Lv et al., 2012; Ma, 2014; Ren et al., 2011; Wang et al., 2007; Zhang et al., 2016). Previous researchers suggested that the Erqis fault zone was active from Carboniferous to Permian (from 320 to 260 Ma; Buslov et al., 2004; Li et al., 2015a; Zhang et al., 2012; Xiao et al., 2015).

2.2. Geology of the Kalasu area

This study is focused on a 37 × 33 km^2 area called "*Kalasu*" (47°35′38″N, 88°20′18″E) in the central part of the Qiongkuer-Abagong terrane (terrane 4 in Figs 1 and 2), located to the southeast of the Altai city (Fig. 1). Previous studies indicate that the Kalasu area is composed of Cambro-Ordovician turbiditic sediments, Late Silurian to Early Devonian island arc volcano-sedimentary rocks and Middle Devonian marine clastic sedimentary sequences (named as Habahe, Kangbutiebao and Altai formations, respectively; Cai et al., 2011a). All these volcano-sedimentary rocks were metamorphosed, occur as schists and gneisses, and were intruded by abundant granodiorite and minor gabbro (Yang et al., 2011). Low-grade Devonian sediments unconformably overlay the turbidite sequence (see Fig. 2; The Team One of Geological Survey of Xinjiang, 1979; Yang et al., 2011). The turbiditic metasediments are generally unfossiliferous, and their protoliths include fine-grained sandstone, siltstone and shale, intercalated with layers of metavolcanic rocks with basaltic and rhyolitic compostions, and minor marble. Most of these turbiditic rocks underwent high-grade metamorphism. Detrital zircons from the paragneiss of this group are predominantly 451 and 591 Ma old, with peaks at ca. 500 and 485 Ma, and constrained their depositional age of 504 ± 4 Ma (see Fig. 2 and Table 1; Jiang et al., 2010; Long et al., 2007; Yang et al., 2011). Few metamorphic zircon rims on detrital zircons from garnet–sillimanite-bearing paragneiss yielded

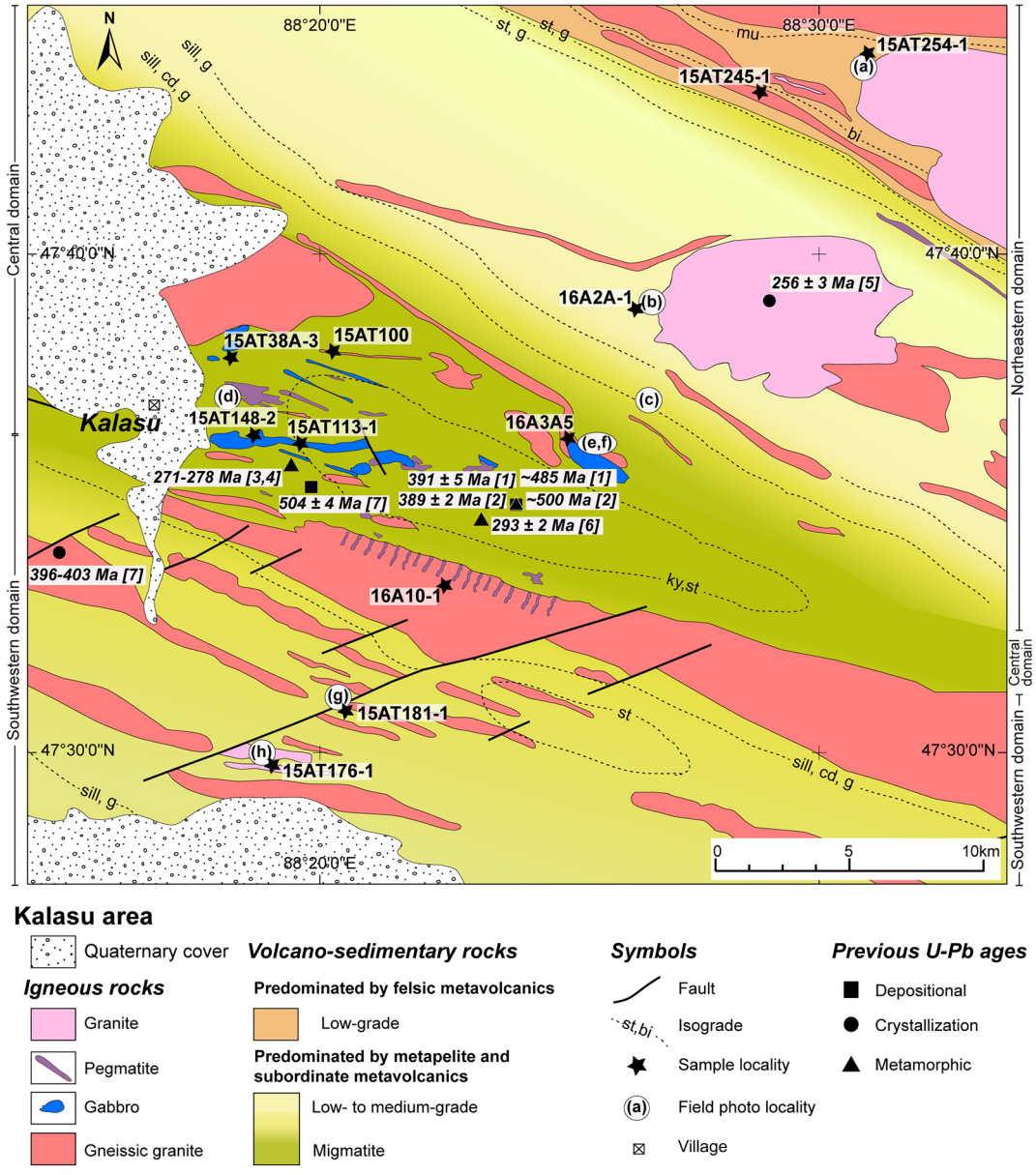

Fig. 2. Simplified lithological map of the Kalasu area, located in the Qiongkuer-Abagong terrane (terrane 4 in Fig. 1), showing distribution of metamorphic zones with mineral assemblage isograds. The location of the samples, field photographs from Fig. 3 and previous zircon ages (compiled in Table 1) are shown. References: [1] Jiang et al., 2010; [2] Long et al., 2007; [3] Tong et al., 2013; [4] Tong et al., 2014a; [5] Wang et al., 2009a; [6] Wang et al., 2009b; and [7] Yang et al., 2011. See text for explanation.

Table 1
Summary of all available U-Pb zircon data reported from the Kalasu area together with new U-Pb zircon ages from this study.

Samples	Rock-type	Dating method	AGES (Ma)			References
			Depositional	Magmatic	Metamorphic	
Northeastern domain						
3084	undeformed granite (Halasu pluton)	U-Pb LA-ICP-MS	–	256 ± 3	–	[5]
15AT254-1	felsic metatuff	U-Pb LA-ICP-MS	–	405 ± 1.4	–	This study
15AT245-1	felsic metavolcano-clastic rock	U-Pb LA-ICP-MS	–	395.4 ± 1.7	–	This study
16A2A-1	metarhyolite	U-Pb LA-ICP-MS	–	388.5 ± 0.9	–	This study
Central domain						
AR12	g-sill-bearing paragneiss	U-Pb LA-Q-ICP-MS (in situ)	~485	–	391 ± 5	[1]
AR12	g-sill-bearing paragneiss	U-Pb LA-ICP-MS	~500	–	389 ± 2	[2]
LT10F-41	UHT metapelitic granulite	U-Pb LA-ICP-MS	–	–	271 ± 5	[3]
LT10F	UHT metapelitic granulite	U-Pb SHRIMP	–	–	278 ± 2	[4]
A152	metapelitic granulite	U-Pb SHRIMP	–	–	292.8 ± 2.3	[6]
×0510–2	g-bearing paragneiss	U-Pb SHRIMP	504 ± 4	–	–	[7]
15AT100–1	migmatite	U-Pb LA-ICP-MS	~516	–	~392	This study
15AT100–2	gneissic granite	U-Pb LA-ICP-MS	–	412.2 ± 1.9	–	This study
15AT38A-3	cd-bearing thin leucosome	U-Pb LA-ICP-MS	–	–	~299–301	This study
15AT148–2	cd-bearing thick leucosome	U-Pb LA-ICP-MS	~507	–	~386	This study
15AT113–1	undeformed gabbro	U-Pb LA-ICP-MS	–	408 ± 2.4	–	This study
15AT113–1	undeformed gabbro	U-Pb LA-ICP-MS	–	279.8 ± 6.0	–	This study
16A3A5	gneissic granite	U-Pb LA-ICP-MS	–	279.1 ± 0.7	–	This study
Southwestern domain						
X0497-4	mylonitic granite	U-Pb LA-Q-ICP-MS	–	402.7 ± 2	–	[7]
X0498-1	mylonitic granite	U-Pb LA-Q-ICP-MS	–	395.7 ± 1.5	–	[7]
X0499-3	mylonitic granite	U-Pb LA-Q-ICP-MS	–	404.3 ± 1.7	–	[7]
X0500-1	mylonitic granite	U-Pb LA-Q-ICP-MS	–	406.2 ± 1.2	–	[7]
X0507-8	mylonitic granite	U-Pb LA-Q-ICP-MS	–	407.5 ± 1.8	–	[7]
16A10-1	gneissic granite	U-Pb LA-ICP-MS	–	402.4 ± 1.4	–	This study
15AT181-1	amp-bearing paragneiss	U-Pb LA-ICP-MS	~492	–	~374	This study
15AT176-1	ep-bearing granite	U-Pb LA-ICP-MS	–	410.5 ± 6.1	–	This study
15AT176-1	ep-bearing granite	U-Pb LA-ICP-MS	–	283.7 ± 1.9	–	This study

ages at ca. 391 to 389 Ma (Table 1 and Fig. 2), suggesting Middle Devonian H*T* metamorphism (Jiang et al., 2010; Long et al., 2007). In addition, this turbidite sequence shows anatexis and contains lenses of M/*LP* to UH*T* garnet–cordierite–sillimanite-bearing metapelitic migmatites and granulites (Tong et al., 2014a; Wang et al., 2009b). For the M/*LP* granulite, pseudosection modelling defined a peak metamorphic condition of 5–6 kbar and 780–800 °C (Wang et al., 2009b), while UH*T* granulites show an anticlockwise *P–T* path from 7 kbar and 890 °C to 9 kbar and 970 °C, followed by a post peak cooling at 8–9 kbar and 870 °C (Tong et al., 2014a). Timing of this migmatitization and granulite-facies metamorphism was inferred from U–Pb zircon dating to ca. 292–271 Ma for migmatite and granulite (see Table 1 and Fig. 2; Tong et al., 2013, 2014a; Wang et al., 2009b).

Both Cambrian to Devonian sequences were intruded by a large number of felsic to mafic bodies in the upper crustal levels. Four gneissic granitic samples register U–Pb zircon ages between ca. 396 and 408 Ma (Yang et al., 2011), and an undeformed felsic intrusion gives an U–Pb zircon age of 256 ± 3 Ma (Wang et al., 2009a) (see Table 1 and Fig. 2).

3. Lithology

Four main lithological groups occur in the Kalasu area and show metamorphic grade increasing from north and south to the central area: (1) metavolcano-clastic rocks and tuffs are dominant in the northeast; (2) metapelitic sequence with subordinate metarhyolite constitutes the main lithology of the central and southwestern part, (Fig. 2); (3) gneissic granitoids crop out over the whole area; and (4) several bodies of gabbro and pegmatite are scattered in the central part (see Figs 2 and 3 as lithological details).

The northeastern domain is characterized by weakly deformed fine-grained tuff or medium- to fine-grained pyroclastic rocks, with centimetre to meter-scale oriented quartz veins (sample 15AT254-1; Fig. 3a). The main minerals in metatuffs (e.g. sample 15AT245-1) are muscovite, quartz, K-feldspar, plagioclase and subordinate biotite, which abundance increases towards SW to the contact with the metapelitic sequence. The metapelitic sequence in the northeastern part is locally interbedded with layers of metarhyolite (e.g. sample 16A2A-1), metatuff, minor marble and amphibolite (Fig. 3b) and is intruded by undeformed coarse-grained porphyritic granite. The metamorphic degree increases to the central part, in the NE the metapelites are represented by biotite schists with local occurrence of garnet and staurolite (Fig. 2) and towards SW, they grade into biotite paragneisses with garnet and/or sillimanite (Fig. 3c; detail photo). Metre-scale amphibolite layers are parallel to the foliations of the paragneiss.

The central domain is dominated by stromatic to nebulitic migmatites with biotite, garnet, sillimanite and cordierite, and occur in up to 10 km wide WNW-ESE trending zone (Fig. 2). Kyanite and staurolite are observed locally. The dominant stromatic migmatites show alternation of quartz–feldspar±cordierite-bearing leucosome layers with biotite ± sillimanite ± garnet ± cordierite-bearing melanosome and mesosome layers (e.g. sample 15AT100-1; Fig. 3d). The melanosome is regularly spaced, whereas the leucosome aggregates and layers vary in size from centimetre to decametre (thin-leucosome: sample 15AT38A-3 and thick-leucosome: sample 15AT148-2). Gneissic granite, undeformed gabbro and pegmatite occur in the migmatites (Fig. 2). The gneissic granite shows strong foliation manifested by preferred orientation of biotite and alignment of feldspar aggregates, crosscut by undeformed melt-bearing shear bands (e.g. sample 15AT100-2; Fig. 3e). Up to 1*5 km^2 undeformed coarse-grained pyroxene gabbro dykes (e.g. sample 15AT113-1) intruded parallel to the foliation of the stromatic migmatites and the gneissic granites (sample 16A3A5; Fig. 3f). These unfoliated gabbroic dykes are accompanied by a large number of smaller, commonly meter-scale gabbroic lenses that are scattered within the migmatites (Fig. 2). The coarse-grained pegmatite veins are composed of quartz, K-feldspar, plagioclase and muscovite, and crosscut the main metamorphic foliation of the migmatites and gneissic granites (Fig. 2).

Fig. 3. Field photographs showing main rock types of the Kalasu area. For localization see Fig. 2. (a,b) northeastern domain: (a) low-grade felsic metavolcano-clastic rock with quartz veins (outlined by black-dashed lines) and (b) low- to medium-grade biotite-schist alternating with metarhyolite. (c–f) Central domain: (c) paragneiss and migmatite at the limit with the northeastern domains; (d) stromatic migmatite displays thin leucosome with cordierite and melanosome with cm-scale garnet; (e) migmatitized gneissic granite, and (f) undeformed gabbro at contact with gneissic granite. (g,h) Southwestern domain: (g) amphibole-bearing paragneiss with and folded quartz lenses, and (h) pink coarse-grained epidote-bearing granite.

The southwestern domain is delineated by a sharp transition from cordierite-bearing migmatites to gneissified granites, amphibolite-facies paragneisses (sample 15AT181-1; Fig. 3g), and rare amphibolite layers of up to several metres width (Fig. 2). Here, the biotite paragneisses contain locally minor garnet and/or sillimanite and/or staurolite. Large number of metre- to

kilometre-scale WNW-ESE elongated intrusions of metagranitoids have strong gneissosity, defined by biotite and recrystallized K-feldspar and quartz aggregates (sample 16A10-1; Fig. 2). Fewer coarse-grained, pink granites are mostly undeformed (sample 15AT176-1; Fig. 3h) or show only locally weak plastic deformation.

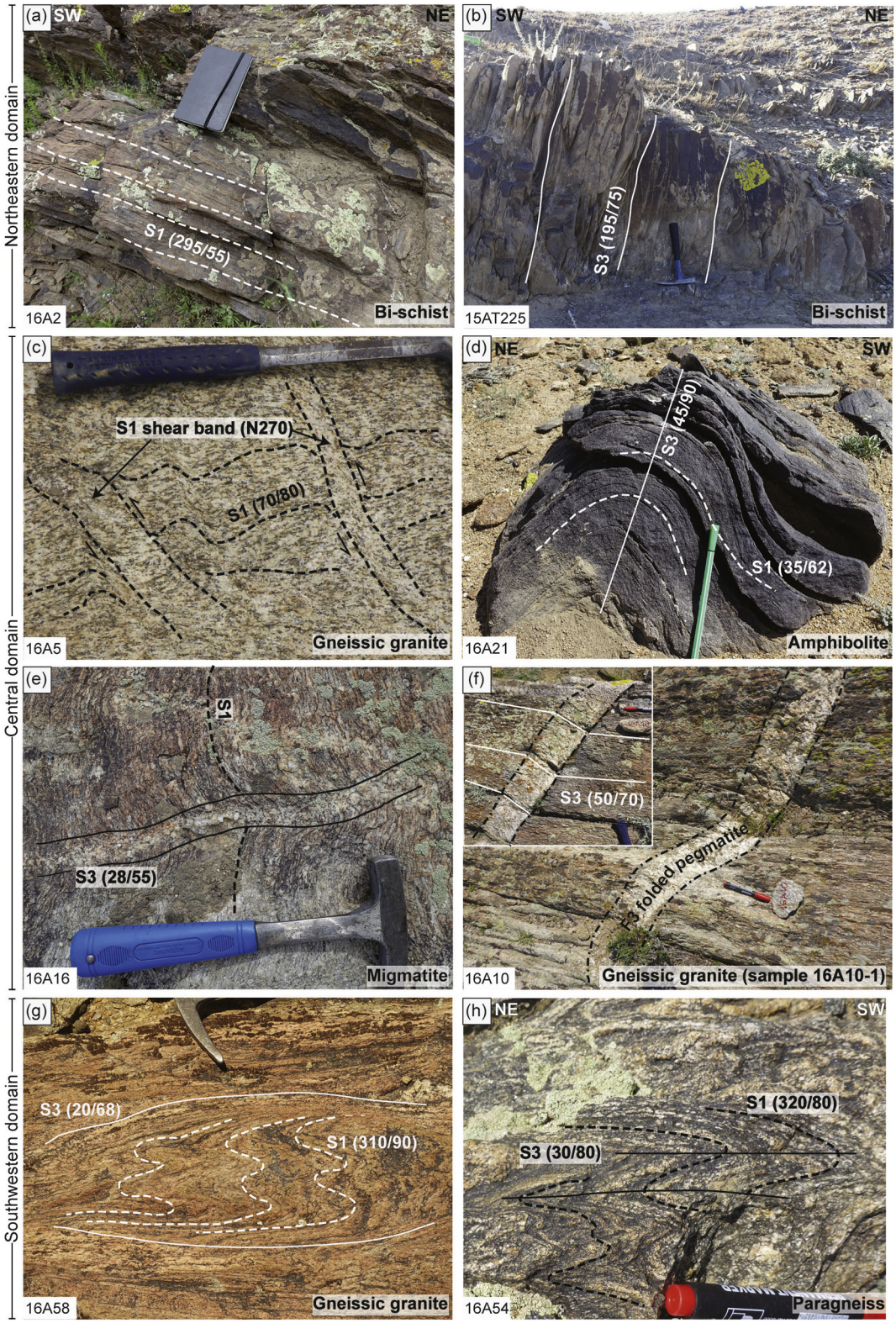

Fig. 4. Structural relationship of the Kalasu area observed along the NE-SW profile. (a,b) northeastern domain: (a) S1 cleavage and (b) tight S3 axial plane in low- to medium-grade bi-schist. (c–f) Central domain: (c) remnants of horizontal S1 foliation and extensional D1 shear zone preserved in the gneissic granite; (d) upright close and asymmetric F3 folds of amphibolite dike affecting the S1 foliation; (e) leucosome parallel to the S3 axial plane and crosscutting the S1 foliation; and (f) pegmatite dike emplaced at high hinge with respect to the penetrative S3 schistosity of gneissic granite and gently folded by D3 deformation showing refraction schistosity inside (upper left inset). (g,h) Southwestern domain: (g) remaining of S1 foliation folded and parallel to S3 axial plane in gneissic granite and (h) S1 foliation in paragneiss refolded by tight D3 folds and crosscut by axial planar S3 cleaveage. Localities of representative pictures are shown on Fig. 5.

4. Deformation

The Kalasu area was affected by three main phases of deformation with variable intensity and degree of preservation as illustrateted in field photographs (Fig. 4) and in a structural map accompanied by an interpretative cross-section and planar and linear structures in stereoplots (see Fig. 5).

D1 deformational phase is characterized by S1 foliation, which is best preserved in the low- to medium-grade metamorphic rocks in the northeastern domain, and locally in the southwestern domain. The stereoplots have maxima showing that the S1 foliation dips moderately to steeply mainly to the NW or locally to the SE (Figs 4a and 5). The NE-SW trending strike and the variable dip of the S1 metamorphic schistosity is interpreted to result from upright NW-SE compression and F2

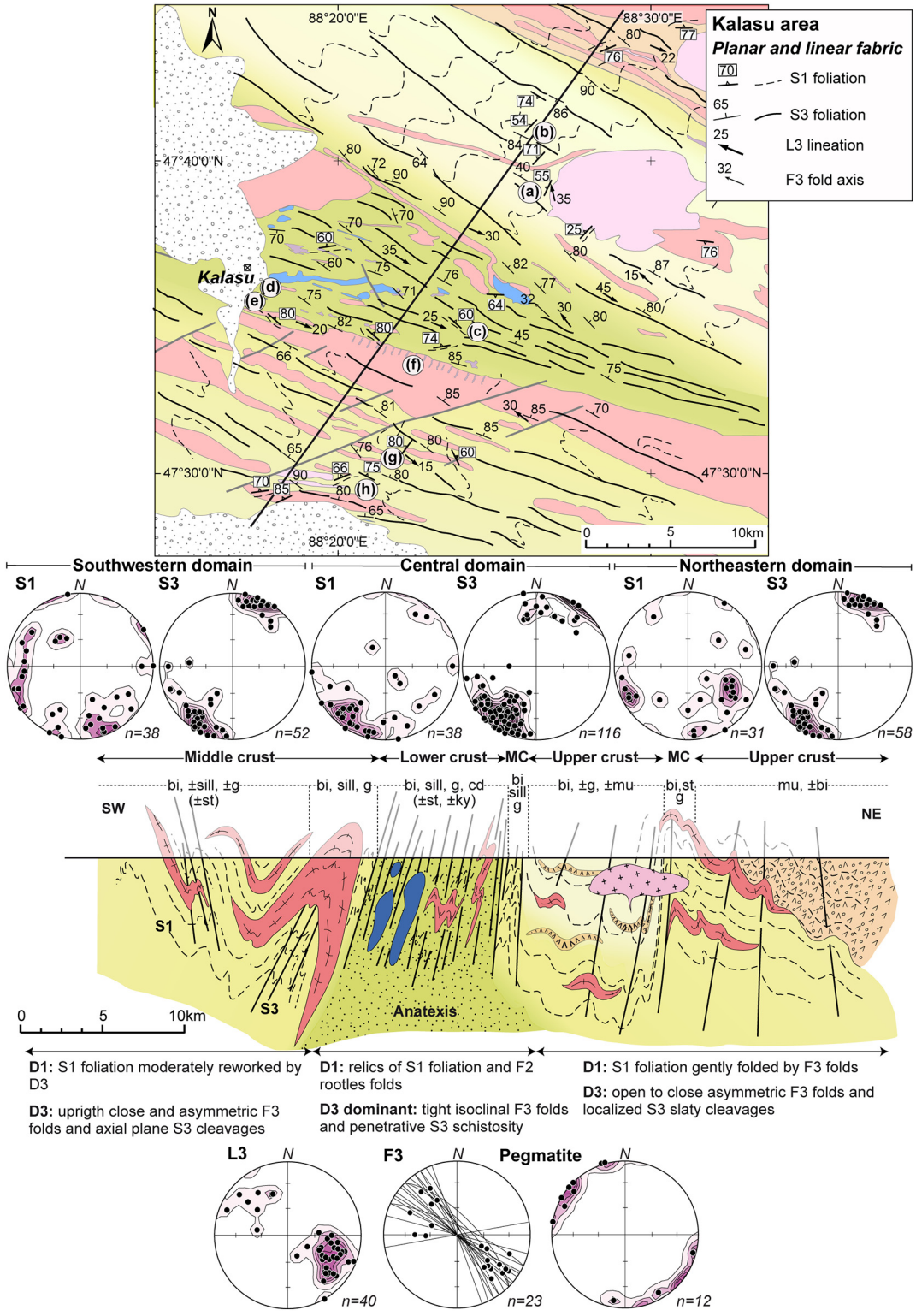

Fig. 5. Structural map and interpretative cross-section showing the main structural features. The stereoplots show orientation of major structural elements (S1 and S3 foliations, L3 lineation, F3 fold axis and pegmatites). (a–h) In the map indicates location of the field photographs from Fig. 4. For the legend see Fig. 2.

folding of the S1 fabric. In this interpretation the D2 deformation is responsible mainly for the reorientation of the originally sub-horizontal S1 fabric, leading to variability in its dip due to F2 folding, but is not associated with penetrative metamorphic stage, thus preserving the S1-M1 metamorphic assemblages. Therefore, in the map it is portrayed as the S1 foliation with NE-SW trending strike (the dashed lines) and the D2 deformation structures are not shown in the map or diagrams (see Fig. 5). At microscopic-scale, the main schistosity S1 is mostly defined by muscovite and biotite in the low-grade metavolcano-clastic rocks and by staurolite and garnet in the medium-grade metavolcano-sedimentary sequence. The S1 foliation is subsequently heterogeneously folded by upright F3 folds with steep NW-SE trending S3 axial plane. In the northeastern domain, the F3 folding is connected with development of low-grade S3 cleavage characterized by oriented growth of muscovite and biotite (Fig. 4b). The intersection between variously dipping S1 and steep S3 foliations resulted in L3 intersection lineation that plunges either to the SE or to the NW (Fig. 5).

In the central high-grade migmatitic domain, the S1 foliation is mainly rotated to NW-SE direction by tight to isoclinal F3 folds. However, relics of W to NW steeply dipping S1 can be observed in the gneissic granites or in some nebulitic migmatites locally preserving the D1 shear bands (Fig. 4c). The NW or SE plunging F3 folds are connected with penetrative NW-SE trending sub-vertical axial planar S3 schistosity (Fig. 4d), which is marked by the presence of cordierite-bearing leucosome and by the orientation of sillimanite, biotite and garnet in the melanosome (Fig. 4e). The S3 is also observed inside pegmatite veins, which intruded perpendicularly to the S3 foliation and were subsequently gently folded by the F3 folds. Here, the geometrical relations between the S3 foliation of the host rocks and of the folded pegmatite veins present features typical for cleavage refraction (Fig. 4f).

In the southwestern domain, the S1 is moderately reworked by upright close and asymmetric F3 folds, but the S1 fabric is still preserved. Some relicts of folded S1 fabrics steeply dipping to the NW are preserved as lozenge-shaped low strain domains inside the S3 fabric in otherwise strongly gneissified granite (Fig. 4g). In general, the S1 foliation is defined by biotite and locally by garnet, sillimanite and staurolite, whereas the axial planar cleavage S3 is marked by oriented sillimanite, biotite and garnet in the paragneisses (Fig. 4h). The L3 lineation marked by sillimanite and biotite plunges either to the NNW or to the SSE (Fig. 5).

The geometry of the D1 and D3 structures is shown in a NE-SW interpretative cross-section and in the associated stereoplots (Fig. 5). Poles to the S1 foliation in the low-grade northeastern domain define a main maximum in the SE quadrant and subordinate measurements in the SW quadrant, indicating that the S1 foliation is steeply dipping predominantly to the NW. The SE maximum of the S1 poles indicates strong upright D2 folding. The SW maximum coincides with the S3 cleavage pole maximum, suggesting rotation of the S1 fabric by the F3 folds and important transposition parallel to the S3 cleavage. Poles to the S1 foliation in the high-grade central domain define a SW and a NE maximum at the periphery of the diagram, similar to that defined by poles of the S3 foliation. All the above evidence indicates that the D3 foliation completely transposes the S1 fabric in high-grade rocks. In the southwestern domain, poles of the S1 define a wide SSE and W maximum located at the periphery of the diagram, and a weak maximum in the NW, indicating that the S1 foliation was only partially transposed by the D3 deformation. The plunge of the L3 lineation and of the F3 fold axes are identical, which means that the L3 represents mainly intersection lineation formed during the F3 folding of variably oriented S1 fabrics.

5. U–Pb zircon geochronology

In order to determine the source provenance of the metavolcano-sedimentary units and to establish a correlation between different structural, metamorphic and magmatic events, zircon was separated from 12 samples (Fig. 2 and Table 2). U–Pb isotope composition was analysed on zircons by Laser Ablation – Inductively Coupled Plasma Mass Spectrometry (LA-ICPMS) at the University of Hong Kong and the Czech Geological Survey in Prague (see details of the analytical method in the Appendix A of the Supplementary data). (See Table 3.)

The U–Pb isotopic data are presented according to the division to the northeastern, central and southwestern domains (see Figs 2 and 5). The U–Pb ages are summarized in Table 1 and the original data are available in the Appendix B of the Supplementary data (Tables B1, B2 and B3). $^{207}Pb/^{206}Pb$ ages are used for zircons older than 1000 Ma, whereas $^{206}Pb/^{238}U$ ages are used for zircons younger than 1000 Ma. The error correlation of $^{206}Pb/^{238}U$–$^{207}Pb/^{235}U$ used in the Concordia and Tera-Wasserburg plots is between 0.85 and 0.95, a value from a long-term statistics of the laboratory. The errors reported are 2σ.

5.1. Northeastern domain

The analysed samples (Fig. 2 and Table 2) include two low-grade felsic metavolcanic rocks (samples 15AT254-1 and 15AT245-1) and an intra-sequence metarhyolite within the low-grade metapelitic sequence (sample 16A2A-1), which may constrain the depositional age of the sequence.

5.1.1. Low-grade felsic metavolcanic rocks (samples 15AT254-1 and 15AT245-1)

The samples 15AT254-1 and 15AT245-1 were collected in the NE part of the northeastern domain, where felsic, weakly metamorphosed and deformed metavolcanic rocks are predominant (Fig. 2 and Table 2). Sample 15AT254-1 is a fine-grained metatuff composed mainly of plagioclase, quartz and muscovite with minor biotite, ilmenite and tourmaline. The muscovite and scarce biotite define gently folded S1 foliation or axial planar S3 cleavage (Fig. 6a). Sample 15AT245-1 is a medium-grained metapyroclastic rock (Fig. 3a) with fabric defined by elongated porphyroclasts of quartz and feldspar in a fine-grained S1 fabric defined by oriented biotite, recrystallized bends of quartz, plagioclase and by weakly oriented muscovite (Fig. 6b). Calcite occurs in some feldspar porphyroclasts (inset in Fig. 6b). Zircon grains from both samples (15AT254-1 and 15AT245-1) have similar characteristics, are moderately pale yellow to colourless and transparent rounded grains to mostly idiomorphic prisms ~150–200 μm long (aspect ratio 1:2 to 1:3). Most of them are broken. Under catodoluminescence (CL), they display mainly low luminescent oscillatory zoning, although other textures, such as homogeneous pattern and sector zoning are present rarely (Fig. 7a, b). For sample 15AT254-1 a total of 100 analyses and for sample 15AT245-1 a total of 40 analyses were performed at the University of Hong Kong. The ages for zircons with high Th/U ratio (>0.1) range from 312 to 520 Ma for sample 15AT254-1 and from 341 to 454 Ma for sample 15AT245-1 (Table B1). The most concordant data for 67 analyses in sample 15AT254-1 and for 13 analyses in sample 15AT245-1 yielded mean ages of 405 ± 1.4 Ma (MSWD = 3.6) and 395.4 ± 1.7 Ma (MSWD = 0.76), respectively (Table 1 and Fig. 7a, b). The remaining analyses that record ages younger than 400 Ma or 395 Ma are attributed to variable radiogenic Pb loss. In addition, twelve of these analyses for sample 15AT245-1 show moderate common Pb contents.

5.1.2. Metarhyolite (sample 16A2A-1)

Sample 16A2A-1 was collected in the central part of the low-grade metavolcano-sedimentary sequence in the northeastern domain, close to the Permian granite intrusion (Fig. 2 and Table 2). This sample corresponds to a metarhyolite interlayered within the metapelitic sequence oriented parallel to the S1 (Fig. 3b). It shows a slaty cleavage defined by biotite and scarce muscovite and contains garnet porphyroblasts with numerous quartz inclusions (Fig. 6c). Zircon grains are usually colourless idiomorphic prisms with variable aspect ratio from 1:2 to 1:4, although some rounded grains are found. CL images reveal complex

Table 2
General description and mineral assemblages of the dated samples.

Sample no	Longitude	Latitude	Sample name	Domains	Mineral assemblages[a]
15AT254-1	88.518	47.734	Low-grade metatuff	Northeastern	mu-q-pl-bi-ilm-tour
15AT245-1	88.479	47.721	Low-grade metapyroclastic rock	Northeastern	q-pl-bi-mu-cal-mt
16A2A-1	88.446	47.654	Metarhyolite	Northeastern	pl-q-bi-mu-(g)-ilm
15AT100-1	88.337	47.634	Migmatite	Central	pl-q-kfs-bi-sill-cd-ilm-mt
15AT100-2	88.337	47.634	Gneissic granite	Central	pl-q-kfs-bi-mu-ilm-mt
15AT38A-3	88.304	47.630	cd-bearing thin leucosome	Central	pl-q-kfs-bi-sill-cd-ilm-mt
15AT148-2	88.310	47.606	cd-bearing thick leucosome	Central	pl-q-kfs-bi-sill-cd-g-ilm-mt
15AT113-1	88.325	47.603	Undeformed gabbro	Central	pl-opx-cpx-ol-ilm-mt
16A3A5	88.416	47.605	Gneissic granite	Central	pl-q-kfs-bi-mu-ilm-mt
16A10-1	88.375	47.555	Gneissic granite	Southwestern	pl-q-kfs-bi-mu
15AT181-1	88.341	47.513	amp-bearing paragneiss	Southwestern	pl-q-bi-amp-ilm-sph
15AT176-1	88.324	47.498	ep-bearing granite	Southwestern	pl-q-bi-ep-ilm-mt

[a] Mineral abbreviations used are: pl = plagioclase, kfs = K-feldspar, q = quartz, bi = biotite, amp = amphibolite, cd = cordierite, sill = sillimanite, g = garnet, ol = olivine, opx = othopyroxene, ep = epidote, sph = sphene, ilm = ilmenite, mt = magnetite, cal = calcite, tour = tourmaline (Holland and Powell, 1998).

textures, from oscillatory to homogenous patterns with a varied luminescence from core to rim (Fig. 7c). A total of 67 spots were analysed at the Czech Geological Survey, yielding $^{206}Pb/^{238}U$ ages of 274–439 Ma (Table B1). Among the 67 analyses, 22 concordant data yield a weighted mean age of 388.5 ± 0.9 Ma (MSWD = 0.76; Table 1 and Fig. 7c), interpreted as the crystallization age of the rhyolite. The remaining 45 analyses show different degree of discordance and the effect of lead loss.

5.2. Central domain

Six samples were collected in the high-grade central domain (Fig. 2). These involve a migmatite (15AT100-1) at contact with a gneissic granite (15AT100-2), a thin centimetre scale cordierite-bearing leucosome (15AT38A-1), a thick cordierite-bearing leucosome (15AT148-1), an undeformed gabbro (15AT113-1) and a gneissic granite (16A3A5) (Table 2).

5.2.1. Migmatite (sample 15AT100-1)

The sample 15AT100-1 is a stromatic migmatite with well-foliated fine-grained melanosome alternating with coarse-grained leucosome. Melanosome is composed of abundant biotite and fibrolitic sillimanite oriented mostly parallel to the S3 foliation. However, some sillimanite and biotite are also oriented along the S1 in the limbs of the F3 folds. Leucosome consists of coarse-grained plagioclase, K-feldspar, quartz, biotite and cordierite (Fig. 8a). Accessory minerals include zircon, monazite, ilmenite and magnetite. Zircon grains are mostly pale yellow to colourless and sub-rounded grains, idiomorphic prisms are subordinate. The CL images show cores surrounded by thin irregular dark to grey rims (Fig. 9a). The cores have variable textures, from homogeneous patterns to oscillatory and sector zoning, with variable luminescence. These characteristics, along with their high Th/U ratio (>0.1; Table B2), suggest that the cores likely represent former magmatic zircons, which were transported and eroded, and subsequently overgrew during metamorphism. In order to determine the source provenance, 100 analyses were performed on the cores at the University of Hong Kong, of which 90 analyses yield concordant ages from 379 to 2020 Ma (in a range of concordance of 95% to 105%; Table B2). Most of the analyses performed on the sample 15AT100–1 yield a major Cambrian peak at ca. 516 Ma, and two secondary clusters are observed at Neoproterozoic (ca. 682–900 Ma) and Palaeoproterozoic (ca. 1768–2020 Ma). The youngest population is represented by two Devonian zircon cores with ages of ca. 379 and 399 Ma (see Fig. 10a and Table 1). To determine the age of high-grade metamorphism, 33 analyses were carried out in the thin dark CL rims at the Czech Geological Survey, yielding concordant ages between 384 and 1471 Ma, interpreted as inherited, and three younger ages with Th/U < 0.1 at around 300 Ma are interpreted to record timing of metamorphism (see blue ellipse in Fig. 10a and Table B2).

5.2.2. Gneissic granite (sample 15AT100-2)

Sample 15AT100-2 is a coarse-grained metagranitoid composed of plagioclase, quartz, K-feldspar and biotite, with accessory minerals of zircon, ilmenite and magnetite. The biotite is oriented parallel to the S1 and to the axial planar S3 cleavage of the F3 folds (Fig. 8b). Zircons from this sample are big and numerous. They are pale yellow to colourless elongated prisms with rounded terminations, variable aspect ratio (between 1:2 to 1:4) and with small inclusions. Under CL, zircons display broad moderately low to high luminescent oscillatory zones typical of magmatic origin, and few grains show less luminescent homogeneous cores (Fig. 11a). No metamorphic rim was observed. Among the 40 grains analysed at the University of Hong Kong, thirty-eight analyses yield concordant ages between 400 and 492 Ma (Table B2). The best estimate for the age was obtained from 31 analyses, yielding a mean age of 412.2 ± 1.9 Ma (MSWD = 1.8; Fig. 11a and Table 1), interpreted as the crystallization age of the granite.

5.2.3. Cordierite-bearing thin leucosome (sample 15AT38A-3)

Sample 15AT38A-3 is a cm-scale thin leucosome separated from a stromatic migmatite. This sample was taken in order to date the high-grade metamorphism (Fig. 2 and Table 2). The thin leucosome is mainly composed of coarse-grained plagioclase, quartz, biotite, cordierite and K-feldspar alternating with thin medium-grained biotite and fibrolitic sillimanite-rich layers parallel to the S3 foliation; although, some biotite and sillimanite are oriented parallel to the S1 foliation (Fig. 8c). Accessory minerals include zircon, ilmenite and magnetite. Zircon grains are colourless or have a variable shade of brown and yellow. They form usually rounded grains and broken prisms with differently shaped pyramid terminations and aspect ratios between 1:2 and 1:4. CL images reveal two groups of zircons: (1) zircons with a complex texture commonly possess prismatic inherited cores with low- to high-luminescent weakly oscillatory and homogenous zoning, and surrounded by variable less luminescent and homogenous rims (from 25 to 50 μm thick); and (2) zircons show homogeneous and dark luminescence (Fig. 9b). Both the low luminescent and homogeneous rims and homogeneous zircons have low Th/U ratio (<0.1; Table B2), being interpreted as metamorphic overgrowths or recrystallizations. A total of 106 spots were analysed on zircons with clear core-rim structures, whereas 45 analyses were carried out in the homogeneous and dark-CL zircons, at the University of Hong Kong and the Czech Geological Survey. Taking into account the CL textures of both grain types and the different zones, few cores yield the oldest ages, whereas dark rim and homogeneous zircons usually show younger ages. From 106 analyses, twenty-nine concordant ages were obtained in the cores, ranging from 280 to 895 Ma (with 95–105% concordance; Table B2). A small group of the analyses in the cores yield ages from Carboniferous to Neoproterozoic (ca. 376–895; Fig. 10b), and are interpreted as inherited. Most of the cores yield

Table 3
Summary of all available U-Pb detrital and volcanic zircon data reported from Habahe/Kulumiti, Kangbutiebao and Altai formations in Chinese Altai.

Samples	Rock-type	Locations (Cities)	Dating Method	AGES (Ma)			AGE POPULATIONS (Ma)			Grains (n_{total})	References
				Depostional	Crystallization	Metamorphic	Youngest	Main	Oldest		
Habahe/kulumiti formations											
BU6-2	amphibolite	Buerjin-Hanas	U-Pb LA-ICP-MS	–	426 ± 3	389 ± 6[a]	386–394[a]	420–439	465–873[b]	33	[5]
BU14	amp-bearing paragneiss	Buerjin-Hanas	U-Pb LA-ICP-MS	461 ± 13	–	387 ± 8[a]	382–392[a]	440–577	658–744	18	[5]
BU19–3	mica-schist	NW Chonghuer	U-Pb LA-ICP-MS	504 ± 7	–	–	–	460–540	620–1179	74	[6]
CH8	g-mica-schist	N Chonghuer	U-Pb LA-ICP-MS	529 ± 14	–	–	–	460–540	620–2493	69	[6]
BEJ96	g-st-sill-bearing paragneiss	NW Chonghuer	U-Pb LA-Q-ICP-MS	464 ± 11	–	–	–	460–540	620–2179	38	[6]
CH12	g-sill-bearing paragneiss	N Chonghuer	U-Pb LA-ICP-MS	534 ± 9	–	–	–	460–540	620–2503	51	[6]
KK8	g-sill-kfs-bearing paragneiss	Keketuohai	U-Pb LA-Q-ICP-MS	515 ± 14	–	–	–	460–540	700–2358	44	[6]
KK03	mica-schist	S Keketuohai	U-Pb LA-ICP-MS	~515	–	–	–	468–586	721–3087	58	[8]
KK10	migmatite	S Keketuohai	U-Pb LA-ICP-MS	~457	–	384 ± 6[a]	370–401[a]	460–513	659–1513	54	[8]
BH09	siltstone	S Baihaba	U-Pb LA-ICP-MS	~499	–	–	–	465–525	594–2743	33	[8]
KK01	mylonite (Fuyun Fault)	NE Fuyun	U-Pb LA-ICP-MS	~501	–	–	–	429–545	561–2033	73	[8]
LO7BH16	sandstone	Baihaba-Hanas	U-Pb LA-ICP-MS	~491	–	–	431–447	454–533	650–2500	52	[9]
LO7BH27	slate	Baihaba-Hanas	U-Pb LA-ICP-MS	~470	–	–	431–447	459–522	700–2900	63	[9]
LO7BH01	siltstone	Baihaba-Hanas	U-Pb LA-ICP-MS	~476	–	–	431–447	469–525	650–2900	62	[9]
BU-4	g-sill-bearing paragneiss	SW Chonghuer	U-Pb LA-ICP-MS	505 ± 7	–	–	–	479–533	569–2516	35	[11]
BU-5	sill-bearing paragneiss	SW Chonghuer	U-Pb LA-ICP-MS	517 ± 8	–	–	–	480–538	592–2159	31	[11]
BU-13	sill-bearing paragneiss	NW Chonghuer	U-Pb LA-ICP-MS	481 ± 11	–	–	–	446–519	573–2626	31	[11]
BU-14	amp-bearing paragneiss	NW Chonghuer	U-Pb LA-ICP-MS	466 ± 11	–	–	–	426–524	640–2634	35	[11]
BU-19	mica-schist	NW Chonghuer	U-Pb LA-ICP-MS	528 ± 16	–	–	–	477–597	729–936	25	[11]
X0555-7	rhyolite	NW Qinghe	U-Pb SHRIMP-II	–	501.8 ± 7.2	–	–	461–516	941–2001	14	[17]
X0555-7	rhyolite	NW Qinghe	U-Pb LA-ICP-MS	–	501.8 ± 7.3	–	–	462–516	942–2001	20	[17]
12BU73	sill-kfs-bearing paragneiss	W Chonghuer	U-Pb LA-ICP-MS	515 ± 4	–	–	~460	500–550	749–1983	31	[21]
AL07	mica-schist	NW Kuerti	U-Pb LA-ICP-MS	~470–506	–	–	–	465–576	781–2572	54	[16]
AL10	mica-schist	NW Kuerti	U-Pb LA-ICP-MS	~471–516	–	–	–	464–549	766–2555	61	[16]
Kangbutiebao formation											
Abg178	metarhyolite	SE Altai city	U-Pb SHRIMP-II	–	412.6 ± 3.5	–	–	317–488	–	16	[1]
Abg53	metarhyolite	SE Altai city	U-Pb SHRIMP-II	–	408.7 ± 5.3	–	–	372–495	–	13	[1]
Tm51	metarhyolite	SE Altai city	U-Pb SHRIMP-II	–	406.7 ± 4.3	–	–	396–424	–	15	[1]
CH01	metarhyolite	Chonghuer basin	U-Pb LA-MC-ICP-MS	–	385.3 ± 1.2	–	–	379–392	–	24	[2]
CH09	metarhyolite	Chonghuer basin	U-Pb LA-MC-ICP-MS	–	398.1 ± 1.8	–	–	394–458	–	20	[2]
CH25	metatuff	Chonghuer basin	U-Pb LA-MC-ICP-MS	–	405.6 ± 2.2	–	–	321–413	–	20	[2]
DDG01	metarhyolite	N-NW Altai city	U-Pb LA-MC-ICP-MS	–	388.9 ± 3.2	–	–	349–393	–	20	[3]
DDG08	metarhyolite	N-NW Altai city	U-Pb LA-MC-ICP-MS	–	400.7 ± 1.6	–	–	380–420	–	20	[3]
	metandesite	Chonghuer basin	U-Pb LA-MC-ICP-MS	–	398.8 ± 1.3	–	–	317–402	670–788	32	[4]
SW47	metarhyolite	N Fuyun	U-Pb SIMS	–	401 ± 3.1	–	–	395–408	514–2575	18	[7]
SW89	metarhyolite	N Fuyun	U-Pb SIMS	–	401.2 ± 2.7	–	–	392–416	–	20	[7]
TM1	metarhyolite	NE Kuerti	U-Pb SHRIMP-II	–	400.8 ± 8.4	–	–	380–410	–	21	[10]
KK7	metarhyolite	NE Kuerti	U-Pb SHRIMP-II	–	402.2 ± 6	–	–	377–407	–	15	[10]
Ashele	metarhyolite	N Kuerti	U-Pb LA-MC-ICP-MS	–	375 ± 3	–	–	370–385	–	15	[14]
Keyinbulake	metarhyolite	N Kuerti	U-Pb LA-MC-ICP-MS	–	401 ± 4	–	–	394–411	–	15	[14]
KKT 01	metarhyolite	NW Kuerti	U-Pb LA-MC-ICP-MS	–	410.5 ± 1.3	–	–	408–412	–	20	[18]
KKT 09	metatuff	NW Kuerti	U-Pb LA-MC-ICP-MS	–	394.8 ± 1.9	–	–	390–403	–	20	[18]
Tmp-1	metarhyolite	SE Altai city	U-Pb LA-MC-ICP-MS	–	407.3 ± 9.2	–	–	375–407	–	6	[19]
Kkp-7	metarhyolite	S Kuerti	U-Pb LA-MC-ICP-MS	–	407.3 ± 9.2	~339–360	339–360	339–420	–	7	[19]
Altai formation											
AR12	g-sill-bearing paragneiss	SE Altai city[c]	U-Pb LA-Q-ICP-MS (in situ)	~485–506	–	391 ± 5	390–392	451–591	600–2000	29	[5]

Table 3 (*continued*)

Samples	Rock-type	Locations (Cities)	Dating Method	AGES (Ma)			AGE POPULATIONS (Ma)			Grains (n_{total})	References
				Depostional	Crystallization	Metamorphic	Youngest	Main	Oldest		
AR12	g-sill-bearing paragneiss	SE Altai city[c]	U-Pb LA-ICP-MS	~500	–	389 ± 2	388–391	456–547	553–2042	58	[8]
×0510–2	g-bearing paragneiss	SE Altai city[c]	U-Pb SHRIMP-II	504 ± 4	–	–	–	488–521	535–2796	24	[10]
A152	metapelitic granulite	SE Altai city[c]	U-Pb SHRIMP	–	–	292.8 ± 2.3[a]	–	280–300	–	9[a]	[15]
LT10F-41	UHT metapelitic granulite	SE Altai city[c]	U-Pb LA-ICP-MS	491 ± 46	–	271 ± 5	260–280	450–500	740–1150	35	[12]
LT10F	g-opx-sill-cd granulite	SE Altai city[c]	U-Pb SHRIMP	–	–	278 ± 2	–	270–285	–	33	[13]
08AL11	paragneiss	N Buerjin	U-Pb LA-ICP-MS	466 ± 8	–	–	–	419–470	485–2528	54	[20]
04TW3	mylonitized paragneiss	Mayinebo	U-Pb SHRIMP	525 ± 13	–	463 ± 15	425–473	486–553	817–2251	21	[20]
0410TW3	migmatite	NW Fuyun	U-Pb SHRIMP	–	–	283 ± 4	–	275–290	–	17	[20]

References: [1] Chai et al., 2009; [2] Chai et al., 2012; [3] Geng et al., 2012; [4] Guo et al., 2015; [5] Jiang et al., 2010; [6] Jiang et al., 2011; [7] Liu et al., 2010; [8] Long et al., 2007; [9] Long et al., 2010; [10] Shan et al., 2011; [11] Sun et al., 2008; [12] Tong et al., 2013; [13] Tong et al., 2014a; [14] Wan et al., 2011; [15] Wang et al., 2009b; [16] Wang et al., 2014a;[17] Yang et al., 2011; [18] Yang et al., 2018; [19] Zhang et al., 2000; [20] Zhang et al., 2012 and [21] Zhang et al., 2015. For cities, locations, see Fig. 1.
Abbreviations for minerals: amp, amphibole; kfs, K-feldspar; g, garnet; opx, orthopyroxene; sill, sillimanite; st, staurolite
[a] Zircon rims
[b] Xenocrysts
[c] Samples located in Fig. 2.

Permian ages with a major peak at ca. 299 Ma. From the analyses performed on the dark-CL rims and homogenous-CL zircons, only 12 and 11 analyses, respectively, generate concordant ages from 280 to 336 Ma, yielding a weighted mean age at 295.5 ± 4.2 Ma for 21 analyses. However, the result produces a high MSWD (35) that can be considerably lowered if we consider only eleven spots to calculate the weighted mean, resulting in an age of 300.8 ± 1.9 Ma, with an acceptable MSWD = 2.8 (see $^{206}Pb/^{238}U$ weighted average age plot inset in Fig. 10b and Table 1). The remaining younger analyses are interpreted to result from a Pb loss and are interpreted geologically meaningless. The similarity in age between most of the cores and both the dark-CL rims and homogenous-CL zircons suggests that the cores were almost completely reset during the Permian metamorphism.

5.2.4. Cordierite-bearing thick leucosome (sample 15AT148-2)

Sample 15AT148-2 is from a metre-scale thick leucosome collected from a stromatic migmatite in order to date the high-grade metamorphism (Fig. 2 and Table 2). The leucosome consists of coarse-grained plagioclase, K-feldspar, quartz, biotite, cordierite and garnet, and contains thin layers marked by medium-grained biotite and fibrolitic sillimanite. These thin layers are oriented parallel to S1 and also parallel to axial planar S3 foliation (Fig. 8d). Accessory minerals include zircon, ilmenite and magnetite. Zircon is small (~50–100 μm) and colourless, forms mostly rounded grains and rare idiomorphic and elongated prisms. CL images reveal complex textures, from oscillatory to sector and homogenous patterns with variable CL response (Fig. 9c). These characteristics, along with the high Th/U ratio (>0.1; Table B2), suggest that the cores represent former detrital grains, magmatic in origin. Scarce and thinner luminescent rims are present, but are too small for dating. A total of 139 analyses were performed at the University of Hong Kong and the Czech Geological Survey, from which 96 analyses yield concordant ages (95–105% concordance) ranging from 335 to 2773 Ma (Table B2). Most of the analyses (24 grains) yield Cambrian ages from 490 to 531 Ma with a peak at ca. 507 Ma. Small groups of Proterozoic zircons are determined at ca. 624 Ma, 718 Ma, 790 Ma, 936 Ma, 1053 Ma, 1193 Ma, 1591 Ma, 1738–1763 Ma, 2388 Ma, 2511 and 2773 Ma (Fig. 10c). Younger ages from Ordovician to Permian range from 335 to 480 Ma and yield a younger peak at ca. 386 Ma (Fig. 10c and Table 1).

5.2.5. Undeformed gabbro (sample 15AT113-1)

Sample 15AT113-1 was collected from an elongated mafic dyke emplaced in the high-grade migmatites (Fig. 2 and Table 2). This sample is composed of coarse-grained plagioclase, olivine, clinopyroxene and orthopyroxene, and the accessory zircon, ilmenite and magnetite (Fig. 8e). Microscopically and macroscopically, the sample is undeformed. Zircons show two different types of grains: (1) pale yellow to colourless idiomorphic and elongated prisms with abundant dark inclusions and (2) few small and angular grains. They are generally broken. Under CL, these two types of grains show different textures. The prismatic grains display oscillatory zoning with variable CL response from core to rim, whereas the angular grains are low luminescent and homogenous (Fig. 11b). However, both types of grains have high Th/U ratio (>0.1; Table B2). Among the 69 analyses performed at the University of Hong Kong and the Czech Geological Survey, 44 analyses are from the oscillatory zircon and 25 from the homogenous zircons. The best estimate for the age of the oscillatory zircons was obtained from six concordant analyses, yielding a mean age of 408 ± 2.4 Ma (MSWD = 0.22; Fig. 11b and Table 1). From the angular and CL-homogenous zircons, four concordant analyses yield a mean age of 279.8 ± 6 Ma (MSWD = 3.0; Fig. 11b and Table 1). The difference in textures and age of the two types of zircon could suggest that the gabbro records either two magmatic pulses, or that it was contaminated by crustal rocks at the time of intrusion. However, both hypotheses are unlikely owing to the big span of age between both zircon populations, the large amount of older zircon in the sample, and the undeformed character of the gabbro. Therefore, the Devonian ages are interpreted as the timing of magmatic formation of Devonian lower crust by gabbroic underplating. This lower crust is then remolten and remobilized during Permian *HT-UHT* event leading to emplacement of horblende bearing gabbros in the upper crust.

5.2.6. Gneissic granite (sample 16A3A5)

Sample 16A3A5 is a coarse-grained gneissic granite occurring within the migmatites and intruded by the undeformed gabbro (Figs 2 and 3f and Table 2). This sample consists mainly of quartz, plagioclase and K-feldspar, with minor amount of oriented biotite (Fig. 8f). Accessory minerals include zircon, ilmenite and magnetite. Zircon from this sample is pale yellow to colourless and forms broken prisms and/or rounded grains. Zircons have mostly low luminescent homogeneous pattern, while few grains show oscillatory and sector zoning (Fig. 11c). No metamorphic rim was observed. Among the 85 grains analysed at the Czech

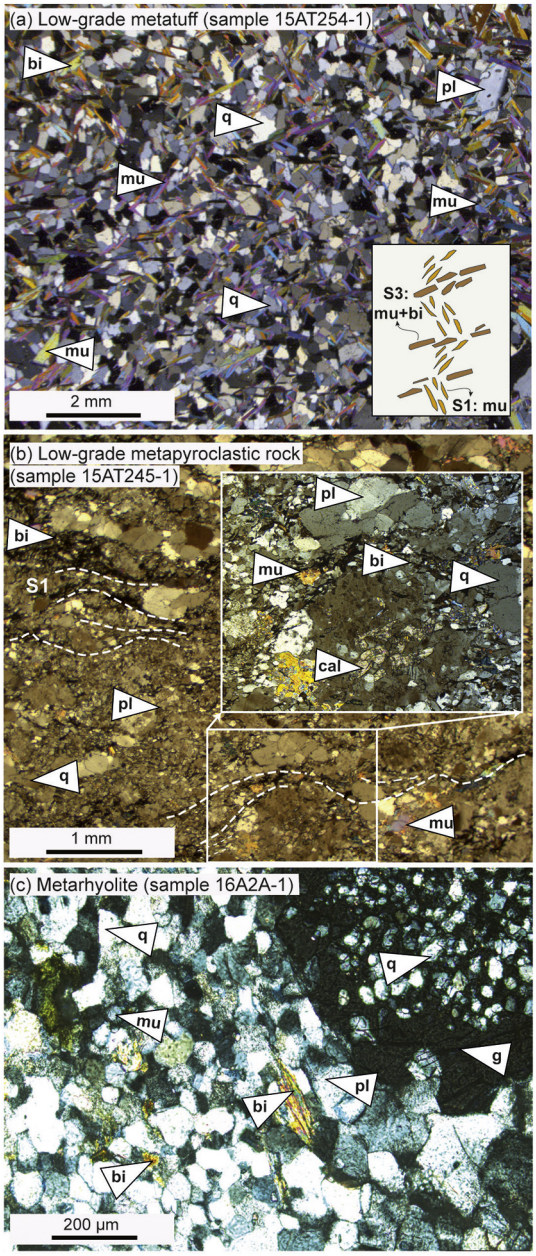

Fig. 6. Microphotographs of the dated rocks from the northeastern domain: (a) Low-grade metatuff rock, fine-grained muscovite and scarce biotite define the S1 foliation folded by open to close upright F3 folds associated with locally developed crenulation S3 cleavage; (b) low-grade felsic metapyroclastic rock, quartz and feldspar porphyroclasts with calcite (see inset) enclosed in a fine-grained schistose fabric of oriented biotite, quartz, plagioclase and muscovite; and (c) metarhyolite, garnet with inclusions of quartz in a fine-grained plagioclase-quartz dominated matrix with biotite and scarce muscovite gently oriented parallel to S1 foliation.

Geological Survey, 50 analyses yield concordant ages between 270 and 419 Ma (90–110% concordance, Table B2). The other analyses gave disconcordant ages from 210 to 402 Ma. The best estimate for the age was obtained from twelve analyses, yielding a mean age of 279 ± 0.7 Ma (MSWD = 0.14; Fig. 11c and Table 1). The younger ages <270 Ma were interpreted as a result of Pb loss, and therefore geologically meaningless. The sparse older ages are interpreted as the age of inherited zircons partially reset and recrystallized during the high-grade Permian metamorphism.

5.3. Southwestern domain

A gneissic granite (16A10-1), an amphibole-bearing paragneiss (15AT181-1) and an epidote-bearing granite (15AT176-1) were collected from this domain (Fig. 2 and Table 2).

5.3.1. Gneissic granite (sample 16A10-1)

Sample 16A10-1 is a coarse-grained gneissic granite at the boundary between the migmatites of the central domain and the paragneisses of the southwestern domain (Fig. 2 and Table 2). It is composed of recrystallized plagioclase, quartz and K-feldspar, and biotite and muscovite oriented parallel to the S3 foliation (Fig. 12a). Zircons are mostly colourless, in form of short prisms with rounded terminations and with aspect ratio between 1:2 to 1:4. Under CL, zircons display broad moderately low to high luminescent oscillatory zones typical of magmatic origin, and few grains show less luminescent homogeneous cores (Fig. 13a). No metamorphic rim was observed. A total of 106 analyses were carried out at the Czech Geological Survey, 39 analyses yield concordant ages ranging from 369 to 459 Ma (94–106% concordance, Table B3). The best estimate for the age was obtained from fifteen analyses, yielding a mean age of 402.4 ± 1.4 Ma (MSWD = 0.63; Fig. 13a and Table 1), interpreted as the crystallization age of the granite. The remaining younger ages were interpreted as a result of Pb loss and therefore geologically meaningless.

5.3.2. Amphibole-bearing paragneiss (sample 15AT181-1)

Sample 15AT181-1 is a medium-grained amphibole-bearing paragneiss, collected in the area of medium-grade metavolcano-sedimentary sequence (Figs 2 and 3g and Table 2). It consists of plagioclase, quartz, amphibole and biotite, with accessory zircon, ilmenite and titanite (Fig. 12b). Both amphibole and biotite are aligned parallel to the S3 foliation. Zircon forms small subhedral to euhedral-rounded grains (~50–200 μm). CL images show mostly oscillatory zoning with variable CL response, from low to high luminescence; however, few grains show homogenous pattern or sector zoning (Fig. 13b). These characteristics and the high Th/U ratio (>0.1; Table B3) suggest that the zircons represent former detrital grains, magmatic in origin. Some zircons show a scarce and thin irregular dark to grey rims in CL images, which are too thin for dating. A total of 100 analyses were performed at the University of Hong Kong, from which 87 yield concordant ages from 303 to 2597 Ma (95–105% concordance, Table B3). Most of the grains provide two main peaks between ca. 357 and 584 Ma with sparse Proterozoic peaks between ca. 635–2601 Ma. The most prominent peak at ca. 492 Ma is defined by 38 grains and the second major peak at ca. 374 Ma is defined by 20 grains. Two Carboniferous peaks are located at ca. 303 and 327 Ma (Fig. 13b and Table 1).

5.3.3. Epidote-bearing granite (sample 15AT176-1)

Sample 15AT176-1 is a coarse-grained granite collected from a small and elongated body within the medium-grade paragneisses (Fig. 2 and Table 2). It is composed of plagioclase, K-feldspar, quartz, biotite, muscovite and epidote, and accessory zircon, ilmenite and magnetite. At outcrop scale, most of the rocks appear as undeformed (Fig. 3h) but under the microscope, biotite is weakly oriented in the S3 fabric and quartz and feldspar are weakly recrystallized (Fig. 12c). Zircon forms big elongated prisms with differently shaped pyramid terminations and length/width ratios between 1:2 and 1:4. Under CL, most zircons display moderately luminescent oscillatory zones typical of magmatic origin; however, few grains have less luminescent homogeneous cores (Fig. 13c). No metamorphic rims were observed. Forty analyses were carried out at the University of Hong Kong, yielding two groups of concordant ages between 279 and 410 Ma (Table B3). The older ages are from fractured cores and yield a mean age of 410.5 ± 6.1 Ma

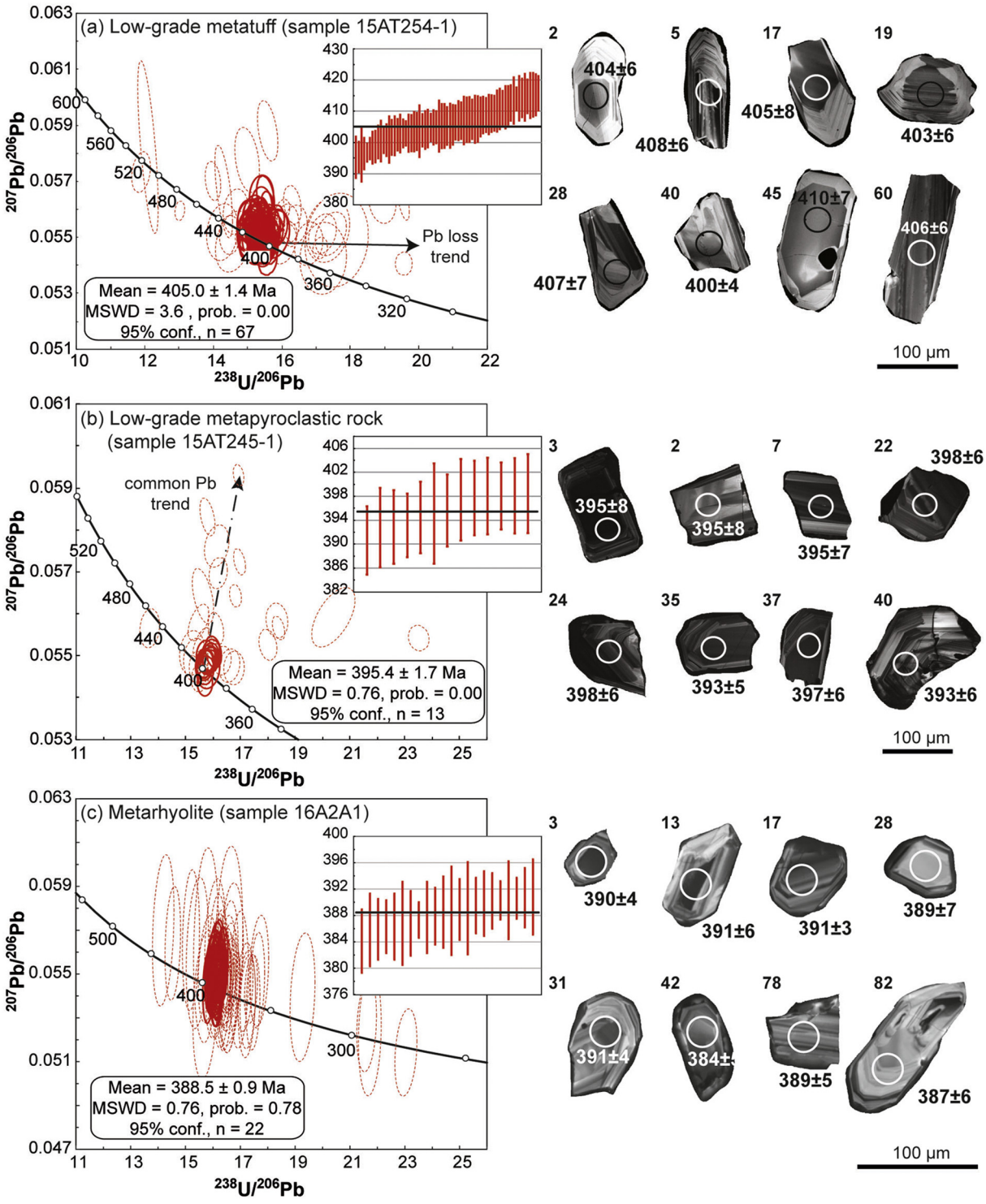

Fig. 7. Tera-Wasserburg diagrams and representative catodoluminescence (CL) images of LA-ICPMS zircon from samples of the northeastern domain: (a) low-grade metatuff (sample 15AT254-1); (b) low-grade felsic metapyroclastic rock (sample 15AT245-1) and (c) metarhyolite at contact with biotite-schist (sample 16A2A1). Locations of LA-ICPMS analysis are shown, the numbers correspond to $^{206}Pb/^{238}U$ ages obtained and to the spot number in Table B1 of the Supplementary data. Error ellipses and error bars are 2σ.

(MSDW = 2.2, n = 5), whereas the younger ages yield a mean age of 283.7 ± 1.9 Ma (MSWD = 1.16, n = 9; Fig. 11c). Some younger ages are interpreted as due to moderate common Pb content and are therefore geologically meaningless. The age of 284 Ma is interpreted as the crystallization age of the epidote-bearing granite (Table 1). The age of 410 Ma is interpreted as the age of xenocrysts due to re-melting or contamination from the Devonian granites that previously intruded in the area.

6. Interpretations and discussion

6.1. Metamorphic and structural evolution of the Kalasu area

The metavolcano-sedimentary rocks and the granitic gneisses can be regarded as a continuous metamorphic sequence with metamorphic grade increasing from the greenschist facies in the northeastern domain through amphibolite facies to migmatitization and granulite facies in

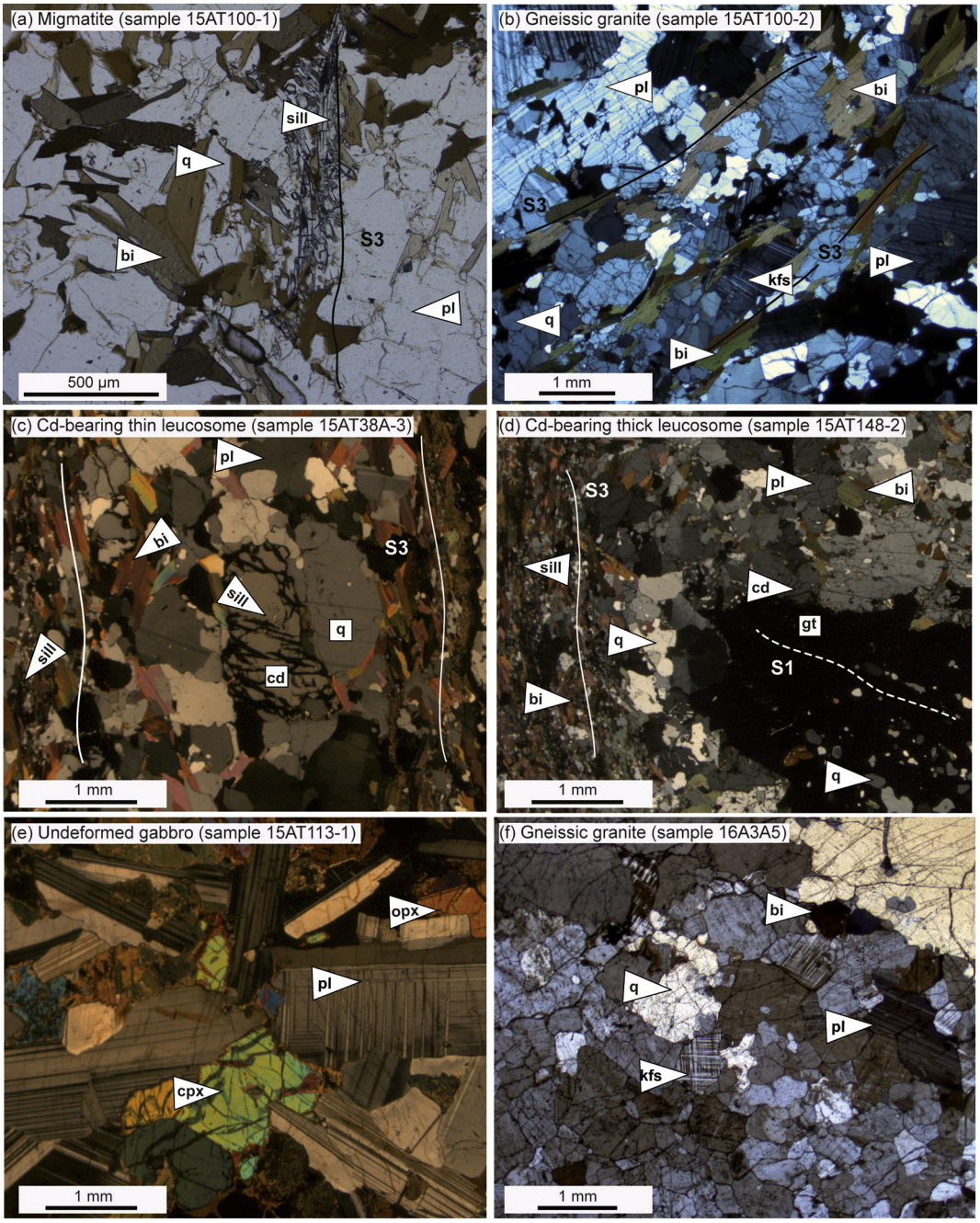

Fig. 8. Microphotographs of the dated rocks from the central domain: (a) migmatite with biotite and sillimanite oriented along the axial planar S3 foliation of the F3 folds; (b) gneissic granite with the axial planar S3 foliation defined by biotite; (c) thin leucosome with coarse-grained cordierite and biotite, and thin biotite and sillimanite layers oriented parallel to the S1 and the axial planar S3 foliation of the F3 folds; (d) thick leucosome with coarse-grained garnet, biotite and cordierite, and thin biotite and sillimanite layers oriented parallel to the S1 limb and the axial planar S3 foliation of F3 folds; (e) undeformed gabbro composed of coarse-grained orthopyroxene, clinopyroxene and subidiomorphic plagioclase; and (f) medium- to coarse-grained gneissic granite composed of quartz, plagioclase, K-feldspar and biotite.

the central domain and then decreasing again to amphibolite facies in the southwestern domain. In detail, several metamorphic zones can be defined: a narrow muscovite zone and a wide biotite zone in the northeastern domain; garnet, staurolite and sillimanite zone in the southwestern domain; and a sillimanite-cordierite–K-feldspar zone in the central domain (see Fig. 2).

Three phases of deformation (D1–D3) were recognized within all domains of the study area (see Figs 4 and 5). The earliest deformation (D1) is characterized by a sub-horizontal S1 foliation (Fig. 2). The presence of extensional shear bands associated with the S1 fabric in partially molten gneissic granite (Fig. 4c) of the central domain indicates important layer perpendicular shortening of deep crustal rocks (Cosgrove, 1997). The S1 foliation was not transposed during D2 deformation but only rotated by NE-SW open to tight and upright F2 folds in fold limbs. This interpretation is in accordance with studies from other areas of the Chinese Altai (Zhang et al., 2015). Such a structural template was subsequently reworked by orthogonal D3 deformation. These conclusions are mainly drawn from opposite dip measurements of NE-SW striking S1 fabrics coming from the northeastern and southwestern domains and the opposite NW or SE plunges of the F3 folds and L3 intersection lineations (Fig. 5).

The D3 is characterized by NW-SE moderately steeply plunging open to close F3 folds, steeply dipping S3 axial planes and S3 cleavage and foliation (Fig. 5), which is delineated by cordierite–K-feldspar-

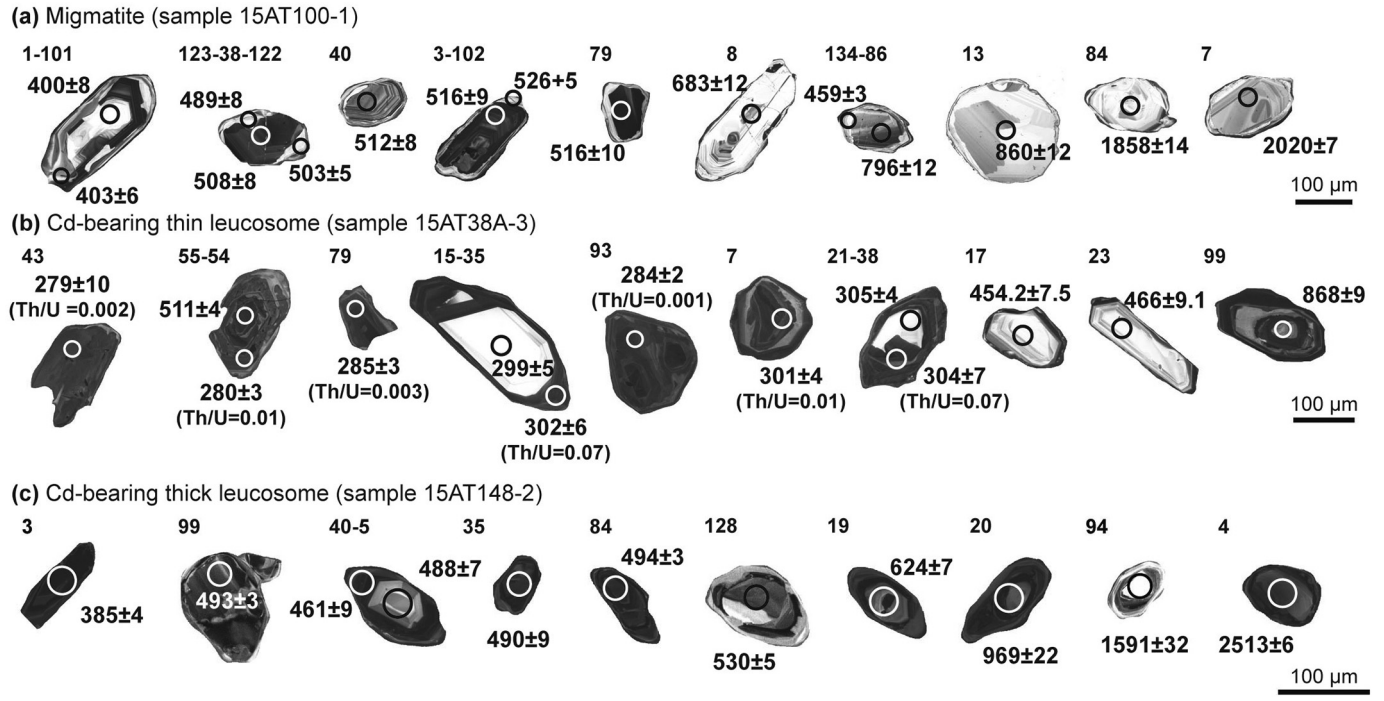

Fig. 9. Catodoluminescence (CL) images of representative zircons from the migmatite (sample 15AT100-1), the cordierite-bearing thin leucosome (sample 15AT38A-3) and the cordierite-bearing thick leucosome (sample 15AT148-2) of the central domain. Locations of LA-ICPMS analysis are shown, the numbers correspond to $^{206}Pb/^{238}U$ ages obtained and to the spot number in Tables B2 of the Supplementary data.

bearing leucosome in the central domain where the S1 foliation is entirely transposed (Fig. 4e). In addition, the S3 fabric in the southwestern and central domains affects pegmatite dykes (Fig. 4f), which were previously dated between ca. 260 to 191 Ma in other areas (e.g. Chen, 2011; Lv et al., 2012; Ma, 2014; Ren et al., 2011; Wang et al., 2007; Zhang et al., 2016). The structural relationships such as refracted weakly developed S3 foliation in pegmatite veins indicate that these veins intruded the sequence during early stages of the D3 in form of tensional gashes. These tensional pegmatite veins were further shortened after solidification of pegmatite magma and subsequently folded by F3 folds during ongoing contraction. Accordingly, we can interpret the D3 structures as a NE-SW contractional deformation phase that affected the whole region with various intensity.

General structure of the study area is characterized by sub-horizontal felsic gneiss sheeted bodies intercalated with metasediments. This layered architecture can originate either from compressional or extensional imbrications of basement gneiss and sedimentary sheets or from intrusions of granite sills parallel to sub-horizontal S1 foliation. As shown by Hanžl et al. (2016), the structural analysis alone is not able to answer these problems and has to be combined with high-resolution geochronology of sedimentary and magmatic rocks to explain complex tectonic and magmatic history.

6.2. Protolith ages, timing of tectono-metamorphic events and associated magmatism

The detrital zircons from the three migmatites studied in the central domain (15AT100-1, 15AT38A-3 and 15AT148-2; Fig. 8a–d) and an amphibole-bearing paragneiss in the southwestern domain (15AT181-1; Fig. 12b) show a predominant population between ca. 460 to 540 Ma (see Figs 10a–c and 13b), clearly indicating that their provenance was dominated by Cambrian to Early Ordovician rocks. This is consistent with the ages previously reported by other authors from other parts of the Chinese Altai (e.g. Jiang et al., 2010, 2011; Long et al., 2007; Shan et al., 2011; Sun et al., 2008; Tong et al., 2013; Zhang et al., 2012; see Table 3 and Fig. 14), implying that the studied metasedimentary sequence was deposited at least 80 Ma prior to Middle Devonian (age of the Altai Formation; e.g. Windley et al., 2002), therefore the previously assigned "Altai Formation" in the study area actually belongs to the Habahe Formation. In contrast, zircons from three low-grade metavolcanic rocks sampled in the northeastern domain (15AT254-1, 15AT245-1 and 16A2A-1; Fig. 6a–c) reveal that the bimodal volcanism erupted between ca. 388 to 405 Ma (Fig. 7a–c), which is consistent with the previous ages assigned to the Kangbutiebao Formation in the Chinese Altai (e.g. Chai et al., 2009, 2012; Geng et al., 2012; Guo et al., 2015; Liu et al., 2010; Shan et al., 2011; Wan et al., 2011; Yang et al., 2018; Zhang et al., 2000; see Table 3).

The earliest granitoids intruded the Cambro-Ordovician sequence during ca. 402 to 412 Ma (15AT100-2 and 16A10-1; Figs 11a and 13a, respectively). Meanwhile, in the northeastern domain, the metavolcano-clastic rocks (ca. 405–395 Ma, 15AT245-1 and 15AT254-1; Fig. 7a–b) and the metarhyolites (388.5 ± 0.9 Ma, 16A2A-1; Fig. 7c) represent lava flows and extrusions and/or synsedimentary depositions of tuffs. The Middle Devonian migmatitization is confirmed by the presence of the younger zircon age population of ca. 392–374 Ma in the migmatites of the central domain (15AT100-1 and 15AT148-2 in Fig. 10a, c) and in the paragneiss of the southwestern domain (15AT181-1 in Fig. 13b). The Devonian migmatitization and deformation are also documented by development of synfolial leucosomes and extensional melt filled shear bands in the central domain (Fig. 4c). In contrast, the metagranites in the southwestern domain show ubiquitous gneissosity parallel to S1 schistosity of surrounding micaschists (Fig. 4g). Altogether, this implies that the emplacement of granitoids preceded the Middle Devonian D1 deep seated migmatitization, deformation and metamorphism in shallow crustal levels.

The preservation of Pre-Devonian zircon ages indicates that the thermal conditions for the Middle Devonian metamorphism and the associated migmatitization did not exceeded the minimum zircon closure temperature (≥700 °C; e.g. Cherniak and Watson, 2001; Hermann and Rubatto, 2003), and thus did not fully reset the zircon U–Pb system. In contrast, the Permian thermal event locally reached ultrahigh-temperature conditions (UHT; >900 °C) in metapelitic granulite (e.g.Li et al.,

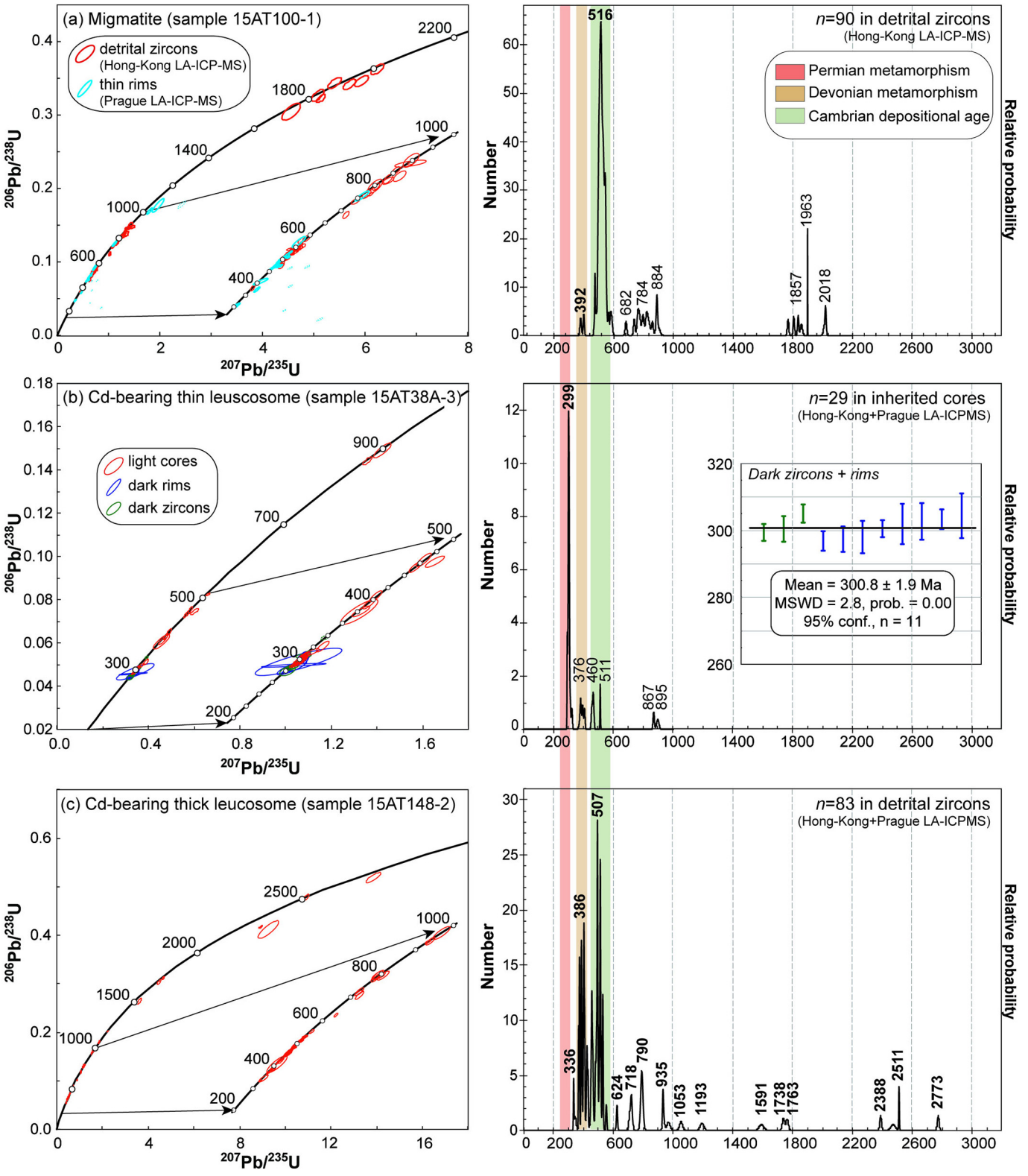

Fig. 10. Concordia diagrams and relative probability density plots of detrital zircons for samples from central domain: (a) migmatite (sample 15AT100-1); (b) cordierite-bearing thin leucosome (sample 15AT138A-3); and (c) cordierite-bearing thick leucosome (sample 15AT148–2). The insets are details of the Concordia age plots and the $^{206}Pb/^{238}U$ weighted average age plot yielded by the metamorphic zircons obtained from the sample 15AT38A-3. Error ellipses and error bars are 2σ. For comparison, the age distribution of the different metamorphic events and maximum depositional age are underlined by colours (see legend).

2004, 2010; Tong et al., 2013, 2014a; Wang et al., 2009b) and exceeded the minimum closure temperature of the zircon. Consequently, in the central domain, the Permian HT to UHT migmatitization overprinted the Devonian metamorphic rocks. This is documented by metamorphic overgrowth and new zircon crystallization in the cordierite-bearing thin leucosome (sample 15AT38A-3; Fig. 9c), yielding a metamorphic age of ca. 299 Ma (Fig. 10b). Similarly, the metagranitoids in the central domain show a dominant Permian zircon population at ca. 280 Ma, with

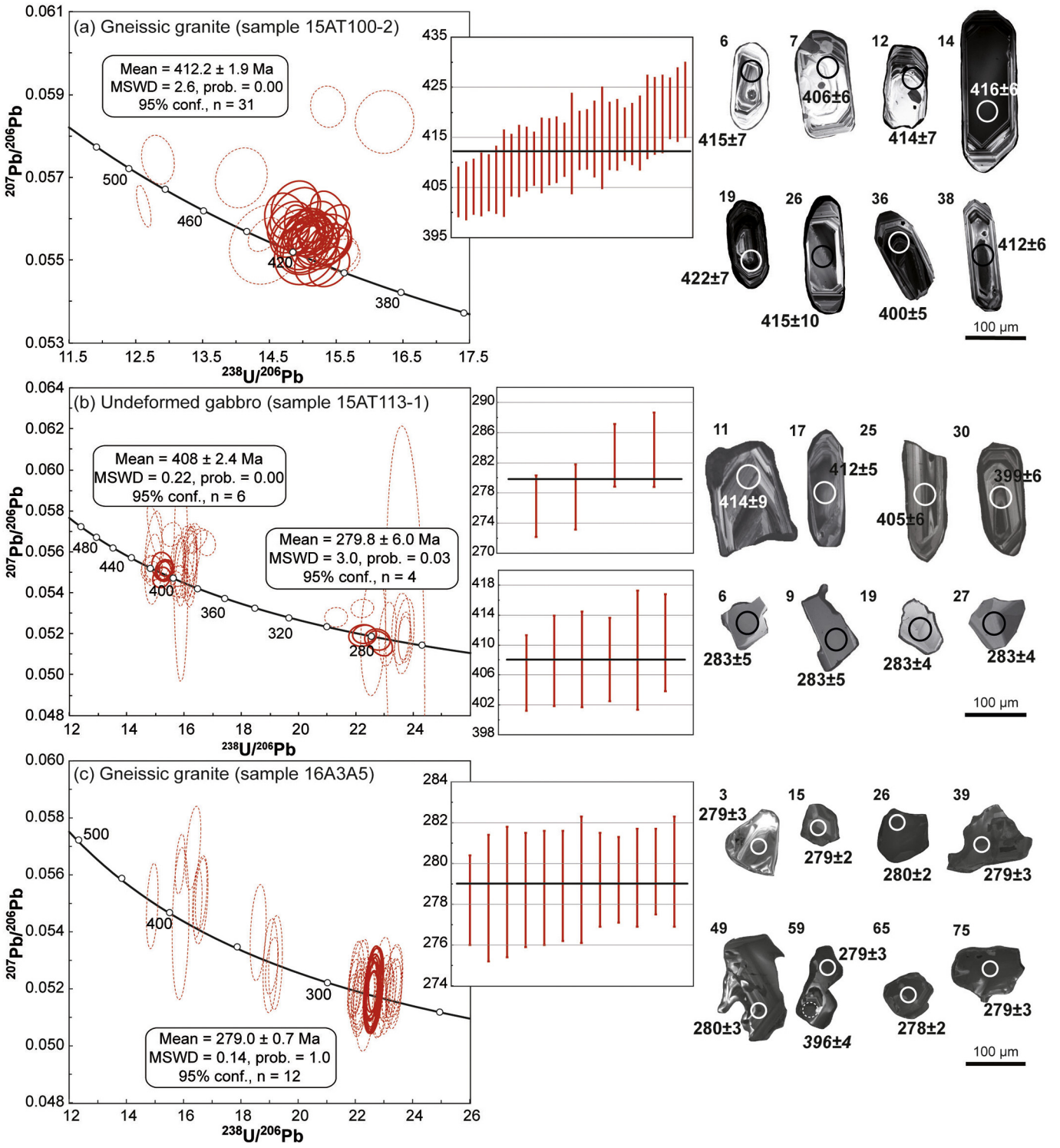

Fig. 11. Tera-Wasserburg diagrams and representative catodoluminescence (CL) images of LA-ICPMS magmatic zircons from the central domain: (a) gneissic granite (sample 15AT100–2); (b) undeformed gabbro (sample 15AT113–1); and (c) gneissic granite (sample 16A3A5). The dashed ellipses represent discordant data and Pb loss, and are excluded from calculation of weighted mean age. The insets are $^{206}Pb/^{238}U$ weighted average age plots. Error ellipses and error bars are 2σ. Locations of LA-ICPMS analysis are shown, the numbers correspond to $^{206}Pb/^{238}U$ ages obtained and to the spot number in Table B2 of Supplementary data.

minor relics of Devonian grains (sample 16A3A5; Fig. 11c). This may imply that Devonian zircons in the magma source of the Permian granitoids were almost entirely reset. Associated with this Permian HT-UHT metamorphism, undeformed gabbros and granite bodies were emplaced at ca. 280 Ma in the central and southwestern domains, respectively (Fig. 2). The undeformed gabbroic sample (15A113-1; Fig. 11b) shows two zircon populations, one Devonian (408 ± 2.4 Ma) and the other Permian (280 ± 6 Ma). This can be interpreted as re-melting of the Devonian mafic lower crust in the Permian time. Widespread Permian melting of the Devonian deep crust is also documented by the 283 ± 1.9 Ma and 410.5 ± 6.1 Ma zircon populations in the epidote-bearing granite in the southwestern domain (sample 15AT176-1; Fig. 13c). Our findings are consistent with the Permian metamorphic ages between ca. 271 to 293 Ma, previously reported by others authors for

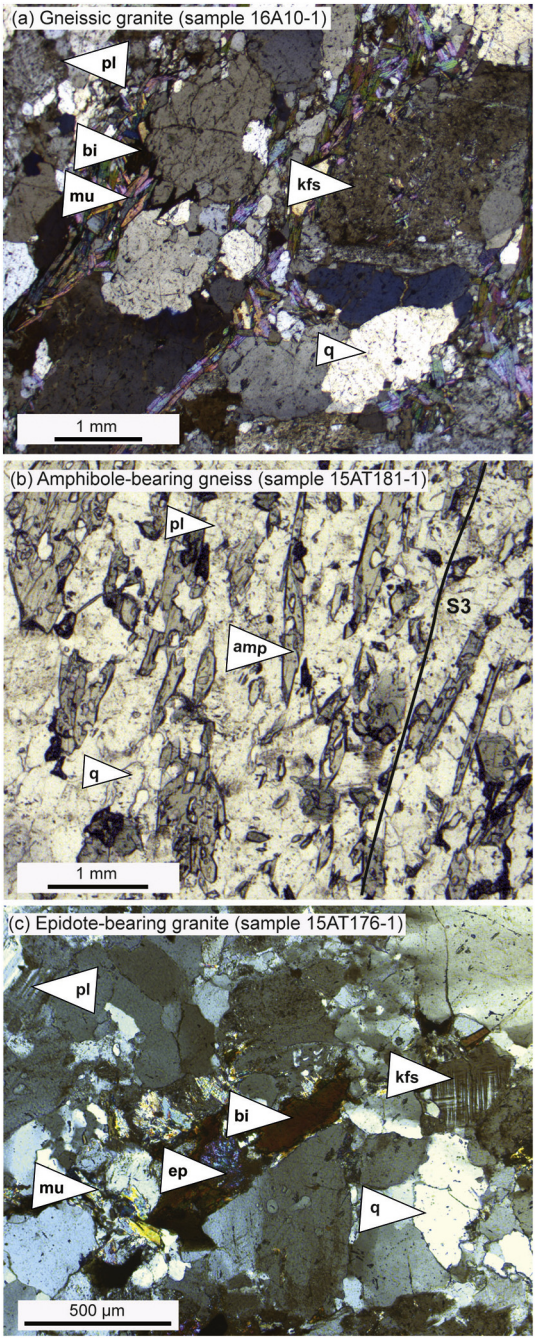

Fig. 12. Microphotographs of the dated rocks from the southwestern domain: (a) medium- to coarse-grained gneissic granite composed of quartz, plagioclase and K-feldspar, with biotite and muscovite parallel to S3 foliation; (b) paragneiss with amphibole parallel to S3 foliation; and (c) pink coarse-grained granite with quartz, plagioclase, K-feldspar, biotite, muscovite and epidote.

the nearby rocks (e.g. Tong et al., 2013, 2014a; Wang et al., 2009b; Zhang et al., 2012; see Fig. 2 and Table 3). Slightly younger Permian zircon ages (e.g. 256 ± 3 Ma) for undeformed granitoids in the northeastern domain have been also reported by previous researchers (Wang et al., 2009a, see Fig. 2 and Table 1).

Combining our data with the U–Pb detrital zircons ages previously obtained in the entire Chinese Altai, we can conclude that the studied "Altai Formation" shares the same maximum depositional age of ca. 500 Ma and a similar age pattern with the Habahe and Kulumiti formations elsewhere (see Fig. 14). This implies that the whole Chinese Altai is mainly composed of the Cambro-Ordovician metavolcano-sedimentary accretionary wedge (e.g. Jiang et al., 2011, 2017; Long et al., 2007, 2010; Sun et al., 2008; Yang et al., 2011) and that the extent of the Devonian volcano-sedimentary sequence is not as large as previously thought (see Fig. 1). The younger age populations reported by our study (15AT100–1, 15AT148-2, 15AT181-1) are thus a result of HT-UHT metamorphism and partial melting (Fig. 14).

6.3. Geodynamic consequences for orogenic architecture of the southern Chinese Altai

The three domains in the Kalasu area can be interpreted as three different orogenic crustal levels according to their metamorphic grade, structural patterns and geochronology: upper orogenic crust in the northeastern domain, middle orogenic crust in the southwestern domain and lower orogenic crust in the central domain (Figs 2 and 15a). The term orogenic crustal position represents the level of a crustal segment during orogeny as defined by Schulmann et al. (2005), and it may not reflect the geophysically and geochemically constrained nature of the crust (Rudnick and Fountain, 1995). According to this model, the orogenic upper crust is defined by low-grade Devonian (ca. 400 Ma) volcano-sedimentary rocks and uppermost part of the Cambro-Ordovician sequence intercalated with Devonian rhyolitic layers all affected by both S1 low-grade fabric and S3 slaty cleavage (Fig. 15a). The orogenic middle crust is defined mostly by well foliated Cambro-Ordovician (ca. 492 Ma) volcano-sedimentary sequence interlayred by highly gneissified Devonian (ca. 400 Ma) granites. All these rocks are affected by amphibolite-facies metamorphism and penetrative D1 deformation locally dated as Middle Devonian (ca. 374 Ma) and also by D3 cleavage (Fig. 15a). The orogenic lower crust is dominated by Cambro-Ordovician (ca. 510 Ma) migmatitic paragneisses and anatectic orthogneisses of Devonian age (ca. 410 Ma) intruded by numerous gabbroic bodies of Permian age (ca. 280 Ma) that resulted from melting of Devonian mafic source. The whole metasedimentary and gneiss sequence is affected by two major schistosity forming high-grade events. Here, the Devonian (ca. 390 Ma) S1 anatectic fabric is almost entirely transposed by Permian (ca. 299 Ma) S3 granulite facies vertical foliation (Fig. 15b).

This study shows complex interplay between the Devonian, Devono-Carboniferous and Permian orogenic events, which affected the Cambro-Ordovician volcano-sedimentary (ca. 516–492 Ma) accretionary wedge and its Devonian cover (see Fig. 15; Jiang et al., 2017). The first Early Devonian magmatic event is connected with emplacement of mafic rocks at the bottom of the crust, intrusion of granitoids in the lower and middle orogenic crust as well as emplacement of rhyolitic bodies in the upper orogenic crust. All the accretionary wedge was subsequently affected by Middle Devonian deformation forming subhorizontal schistosity marked by upwards decreasing metamorphic grade culminating by anatexis in the orogenic lower crust. During this event the sheeted interlayered architecture of the Chinese Altai originated (Fig. 15a). It was intimately associated with important vertical shortening of the whole crust, resulting in horizontal flow and extension of all crustal levels in the whole Chinese and Mongolian Altai (Hanžl et al., 2016; Zhang et al., 2015). Heat source for these two Devonian large-scale magmatic and tectono-metamorphic events is attributed to elevation of asthenosphere above a giant retreating subduction system, similar to that observed in Cascades at the eastern Pacific border (Currie et al., 2004; Jiang et al., 2016). This primary subhorizontal orogenic structure was subsequently affected by important Late Devonian-Early Carboniferous upright NE-SW folding (Lehmann et al., 2017), which modified the architecture of the accretionary wedge and produced alternations of the lower orogenic crust in cores of the antiforms with middle and upper orogenic crust forming large synforms (Fig. 15b).

In contrast, the Permian orogenic event was described only in geochronological, metamorphic and magmatic studies (e.g.,Tong et al., 2013, 2014a; Wang et al., 2014a) and limited mutually disconnected

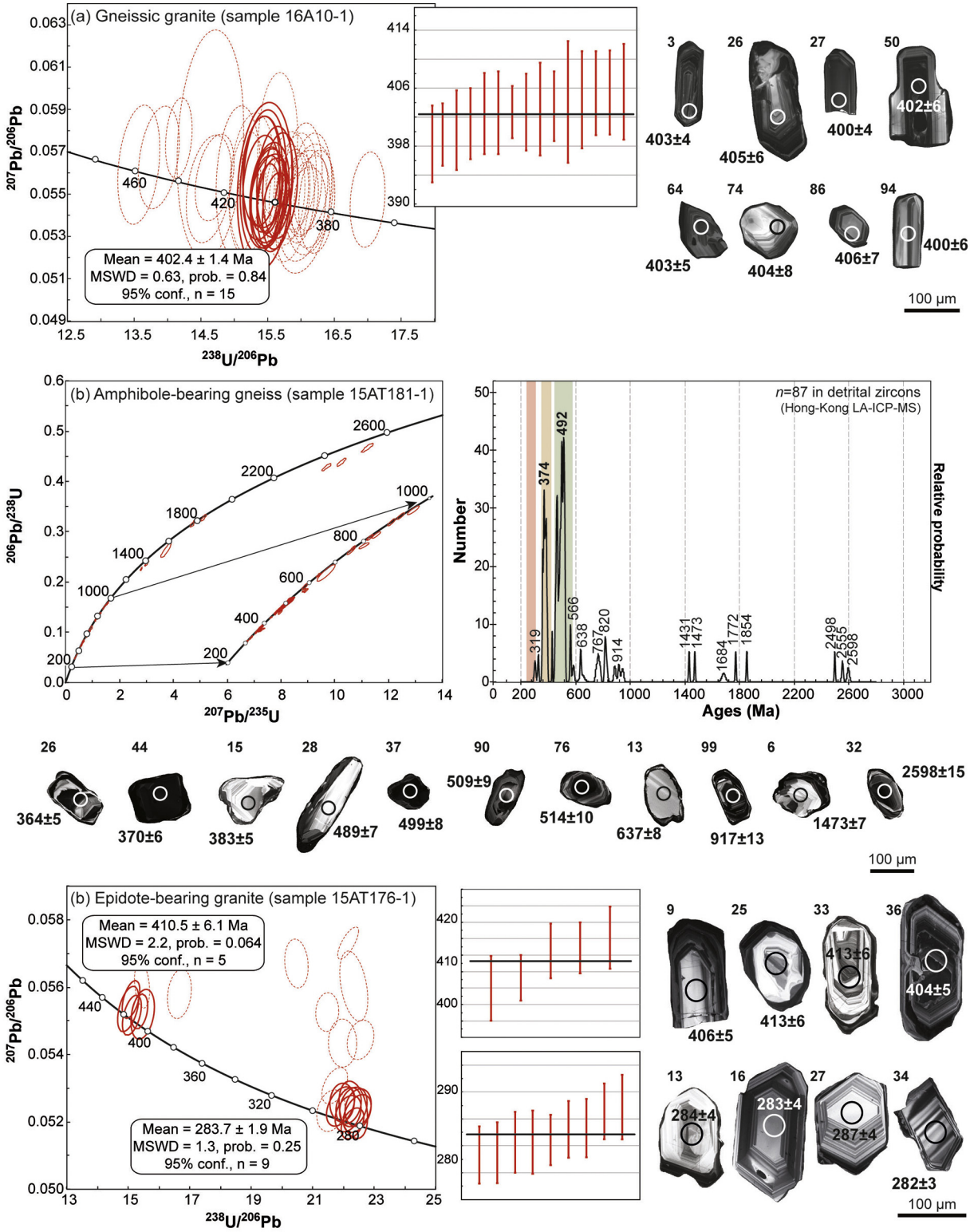

Fig. 13. Tera-Wasserburg and Concordia diagrams together with representative catodoluminescence (CL) images of LA-ICPMS magmatic and detrital zircons from the southwestern domain: (a) gneissic granite (sample 16A10-1); (b) amphibole-bearing paragneiss (sample 15AT181-1); and (c) epidote-bearing granite (sample 15AT176-1). The dashed ellipses represent discordant data and Pb loss, and are excluded from calculation of weighted mean age. The insets are $^{206}Pb/^{238}U$ weighted average age plots for magmatic zircons and relative probability density plots for detrital zircons. Error ellipses and error bars are 2σ. Locations of LA-ICPMS analysis are shown, the numbers correspond to $^{206}Pb/^{238}U$ ages obtained and to the spot number in Table B3 of Supplementary data.

structural studies (Li et al., 2015a, 2016). According to the previous studies, the Permian event was associated with intraplate reworking and reflected an overprinting event attributed to an extensional setting (Briggs et al., 2007; Chen and Han, 2006; Han et al., 2004; Tong et al., 2006, 2014a; Zhang et al., 2012). Here, we show that the Permian event thermally affected and re-melted the Devonian lower orogenic crust of the southern Chinese Altai (see Fig. 15a). We show that the intensive Permian heat input was connected with a contractional event,

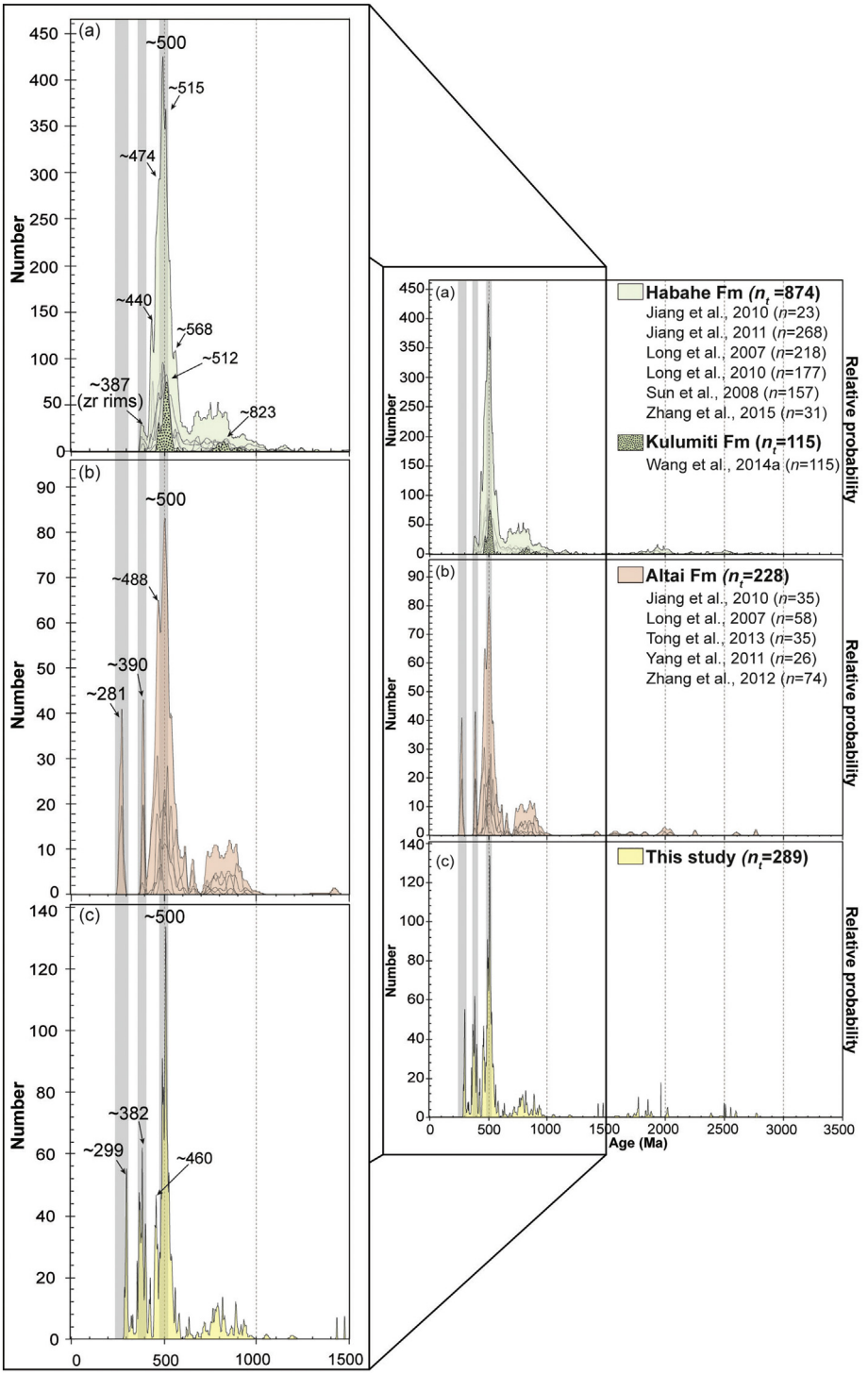

Fig. 14. Comparison of relative probability density plots of previous U–Pb detrital zircon data obtained from Habahe/Kulumiti and Altai formations in Chinese Altai and all new U–Pb data obtained in this study. Shading underlines prominent peaks that are common to zircons in different formations and common to two different metamorphic events that took place during Devonian and Permian.

leading to localized extrusion of migmatitized and granulitized rocks and gabbroic intrusions that are now exposed along a narrow NW-SE trending vertical and tabular high strain zone (Fig. 15b). This extrusion is related to variable intensity of regional-scale upright folding, which decreases from the center to the south and to the north. Such a structural pattern can be interpreted as a result of a Permian deformation perpendicular to the boundary between the Chinese Altai terrane and the Junggar island arc terrane.

The heat source of the Permian event was previously considered to be related to a hot spot or to a large-scale lithospheric extension as a result of a Permian mantle plume (Tong et al., 2013, 2014a; Wang et al., 2014a). Alternatively, some other studies suggested that the Permian mafic rocks including gabbros in the Chinese Altai were not related to any plume because the presence of magmatic hornblende suggests a relatively high water fugacity. In addition, the crystallization temperature (715–826 °C) calculated using Ti-in-zircon thermometry is

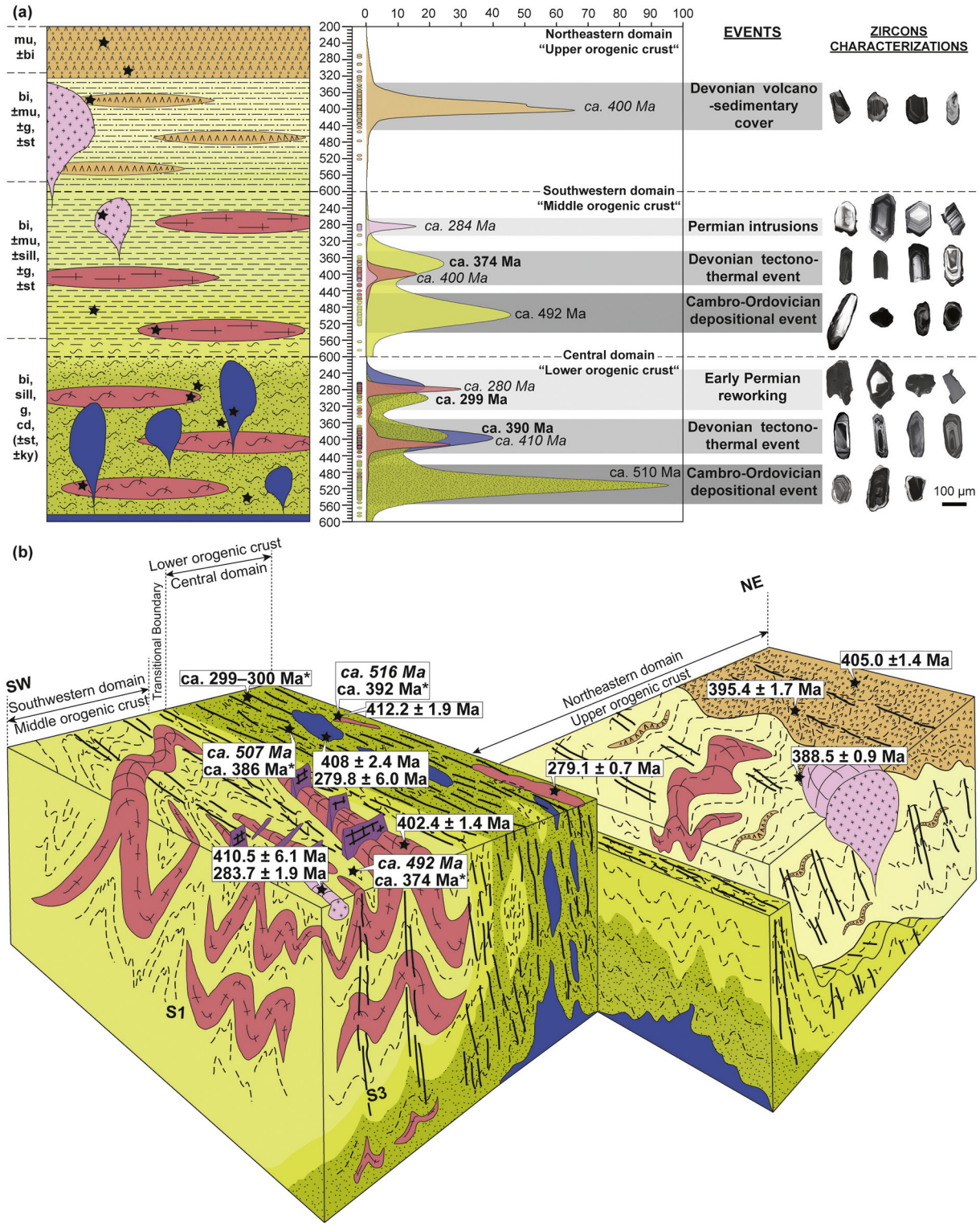

Fig. 15. (a) Vertical scheme of architecture of the Chinese Altai orogenic crust exemplified by the Kalasu area. The subdivision of the Devonian orogenic crustal levels is based on Kernel Density Estimate (KDE) of detritical, metamorphic and magmatic zircon ages (Vermeesch, 2012). Zircon ages of Permian magmatism and metamorphism are also displayed. CL images of typical and representative Cambro-Ordovician, Devonian and Permian zircons are shown in the right panel. (b) 3D interpretative model of the Kalasu area illustrating the main structural relationships in different domains together with the new U–Pb zircon ages from this study. The ages plotted in the map with different font styles and symbols: bold and italic for depositional ages, bold for crystallization ages and bold* for metamorphic ages. The legend is the same as in Fig. 2.

considerably lower than that of a normal mafic melt but consistent with an origin from a water-bearing magma (Wan et al., 2013). These findings rule out the hot spot, large-scale lithospheric extension or mantle plume hypotheses and indicate a thermal regime consistent with accretionary and amalgamation scenarios suggested by Xiao et al. (2015, 2018). Therefore, it is more likely that the accretion/collision of the Junggar arc with the Chinese Altai perturbed the thermal structure of the mantle lithosphere and led to localized elevation of isotherms along narrow deformation zones, parallel to the collisional front. For instance, in Pan-African collisional orogeny, such a model is commonly

applied to explain UHT metamorphism and melting related to the Early Palaeozoic crustal-scale shear zones affecting Late Proterozoic granulitic crust (e.g. Martelat et al., 2000). Here in the CAOB, we show two hot orogenic cycles with time difference >100 Ma. This indicates that similar tectonic processes as in the collisional zones may be an important mechanism for the formation of crustal architecture of accretionary orogenic belts.

7. Conclusions

- The southern Chinese Altai shows that the Cambro-Ordovician accretionary wedge (ca. 520–492 Ma) was extensively affected by the Early Devonian magmatic intrusions in deep crustal levels (ca. 410–400 Ma) associated with formation of a Devonian volcano-sedimentary cover characterized by extrusions of rhyolitic lavas and granites (ca. 405–390 Ma) in the supracrustal levels.
- The whole edifice was affected by Middle Devonian (ca. 390–374 Ma) tectono-metamorphic cycle. The degree of the Middle Devonian metamorphism associated with sub-horizontal S1 fabric increases with depth. This, together with distribution of Devonian metamorphic zircons allows sub-division of the studied region into three orogenic crustal levels: the low-grade upper orogenic crust in the northeastern domain, the middle orogenic crust in the southwestern domain and the lower orogenic crust in the central domain. The Devonian edifice is compatible with important vertical shortening and horizontal flow in all crustal levels.
- The whole system was subsequently affected by regional NE-SW trending upright F2 folding of supposed Late Devonian-Early Carboniferous age with no apparent metamorphism.
- The Devonian orogenic architecture was reworked by Early Permian NE-SW shortening, producing regional NW-SE trending upright F3 folds. This led to localized extrusion of migmatites, anatectic granites and granulite facies rocks (K-feldspar–cordierite–sillimanite) in a crustal-scale vertical, tabular deformation zone. It is also associated with intrusions of gabbros and granites. Zircon dating brackets this event to ca. 300–280 Ma.
- The hot Permian event is interpreted to be related to collision of the Junggar arc with the Chinese Altai terrane that produced a large-scale perturbation of thermal structure of the mantle lithosphere.

Acknowledgement

This study was financially supported by the National Key Research and Development Program of China (2017YFC0601205), the NSF China (41672056, 41230207), the International Partnership Program of the Chinese Academy of Sciences (132744KYSB20160005), the Hong Kong RGC Research Projects (17303415 and 17302317), the HKU grants (201411159173 and 201511159199), and by the Czech Science Foundation (GACR grant 17–17540S). The work forms part of a Ph.D. thesis by A. Broussolle. A 100 Talents Program of the Chinese Academy of Sciences to JYD is also acknowledged. The authors are grateful to Dr. Cai Keda of Xinjiang Institute of Geography and Ecology for field trips assistance. We are also indebted to Dr. Jean Wong from the University of Hong Kong for her help with zircon analyses, the LA-ICPMS operating and the data processing during the course of this work. An anonymous reviewer and Prof. Laixi Tong are thanked for very constructive remarks. This is a contribution to IGCP 662.

Appendix A. Supplementary data

Supplementary data to this article can be found online at https://doi.org/10.1016/j.lithos.2018.06.005.

References

Austrheim, H., 1990. The granulite eclogite facies transition: a comparison of experimental work and a natural occurrence in the Bergen Arcs, western Norway. Lithos 25 (1–3), 163–169.
Beltrando, M., Hermann, J., Lister, G., Compagnoni, R., 2007. On the evolution of orogens: pressure cycles and deformation mode switches. Earth Planet. Sci. Lett. 256 (3–4), 372–388.
Briggs, S.M., Yin, A., Manning, C.E., Chen, Z.-L., Wang, X.-F., Grove, M., 2007. Late Paleozoic tectonic history of the Ertix fault in the Chinese Altai and its implications for the development of the Central Asian Orogenic System. Geol. Soc. Am. Bull. 119 (7–8), 944–960.
Broussolle, A., Štípská, P., Lehmann, J., Schulmann, K., Hacker, B.R., Holder, R., Kylander-Clark, A.R.C., Hanžl, P., Racek, M., Hasálova, P., Lexa, O., Hrdličkova, K., Buriánek, D., 2015. *P–T–t–d* record of crustal-scale horizontal flow and magma-assisted doming in the SW Mongolia Altai. J. Metamorph. Petrol. 33, 359–383.
Burenjargal, U., Okamoto, A., Kuwatani, T., Sakata, S., Hirata, T., Tsuchiya, N., 2014. Thermal evolution of the Tseel terrane, SW Mongolia and its relation to granitoid intrusions in the Central Asian Orogenic Belt. J. Metamorph. Geol. 32, 765–790.
Burenjargal, U., Okamoto, A., Tsuchiya, N., Uno, M., Horie, K., Hokada, T., 2016. Contrasting geochemical signatures of Devonian and Permian granitoids from the Tseel Terrane, SW Mongolia. J. Geosci. 61 (1), 51–66.
Buslov, M.M., Watanabe, T., Fujiwara, Y., Iwata, K., Smirnova, L.V., Safonova, I.Y., Semakov, N.N., Kiryanova, A.P., 2004. Late Palaeozoic faults of the Altai region, Central Asia: tectonic pattern and model of formation. J. Asian Earth Sci. 23 (5), 655–671.
Cai, K., Sun, M., Yuan, C., Long, X., Xiao, W., 2011a. Geological framework and Palaeozoic tectonic history of the Chinese Altai, NW China: a review. Russ. Geol. Geophys. 52 (12), 1619–1633.
Cai, K., Sun, M., Yuan, C., Zhao, G., Xiao, W., Long, X., Wu, F., 2011b. Prolonged magmatism, juvenile nature and tectonic evolution of the Chinese Altai, NW China: evidence from zircon U–Pb and Hf isotopic study of Palaeozoic granitoids. J. Asian Earth Sci. 42 (5), 949–968.
Chai, F.M., Mao, J.W., Dong, L.H., Yang, F.Q., Liu, F., Geng, X.X., Zhang, Z.X., 2009. Geochronology of metarhyolites from the Kangbutiebao Formation in the Kelang basin, Altay Mountains, Xinjiang: implications for the tectonic evolution and metallogeny. Gondwana Res. 16, 189–200.
Chai, F.M., Yang, F.Q., Liu, F., Geng, X.X., Jiang, L.P., Lv, S.J., Jiang, M., Zang., M Chen, B., 2012. Geochronology and genesis of meta-felsic volcanic rocks from the Kangbutiebao formation in Chonghuer basin on southern margin of Altay, Xinjiang. Geol. Rev. 58 (6), 1023–1037 (in Chinese with English abstract).
Chen, J.F., 2011. Geochemistry of the Plate Part in Altai No. 3 Pegmatite and Its Formation and Evolution. A Dissertation Submitted to Graduate University of Chinese Academy of Sciences for the Degree of Master of Philosophy. pp. 1–86.
Chen, L., Han, B., 2006. Geochronology, geochemistry and Sr–Nd–Pb isotopic composition of mafic intrusive rocks in Wuqiagou area, north Xinjiang: constraints for mantle sources and deep processes. Acta Petrol. Sin. 22, 1201–1214 (in Chinese with English abstract).
Chen, B., Jahn, B.M., 2002. Geochemical and isotopic studies of the sedimentary and granitic rocks of the Altai orogen of northwest China and their tectonic implications. Geol. Mag. 139 (1), 1–13.
Chen, H., Yang, S., Li, Z., Yu, X., Xiao, W., Yuan, C., Li, J., 2006. Zircon SHRIMP U–Pb chronology of the Fuyun basic granulite and its tectonic significance in the Altaid orogenic belt. Acta Petrol. Sin. 22, 1351–1358 (in Chinese with English abstract).
Cherniak, D.J., Watson, E.B., 2001. Pb diffusion in zircon. Chem. Geol. 172, 5–24.
Collins, W.J., 2002. Hot orogens, tectonic switching and creation of continental crust. Geology 30, 535–538.
Collins, W.J., 2003. Slab pull, mantle convection, and Pangaean assembly and dispersal. Earth Planet. Sci. Lett. 205, 225–237.
Cosgrove, J.W., 1997. The influence of mechanical anisotropy on the behaviour of the lower crust. Tectonophysics 280 (1–2), 1–14.
Currie, C.A., Wang, K., Hyndman, R.D., He, J., 2004. The thermal effects of steady-state slab-driven mantle flow above a suducting plate: the Cascadia subduction zone and back-arc. Earth Planet. Sci. Lett. 223 (1–2), 35–48.
Dewey, J.F., Ryan, P.D., Andersen, T.B., 1993. Orogenic uplift and collapse, crustal thickness, fabrics and metamorphic phase changes: the role of eclogites. J. Geol. Soc. London, Special Pub. 76 (1), 325–343.
Geng, X.X., Yang, F.Q., Chai, F.M., Liu, M., Guo, X.J., Guo, Z.L., Liu, F., Zhang, Z.X., 2012. LA–ICP–MS U–Pb dating of volcanic rocks from Dadonggou ore district on southern margin of Altay in Xinjiang and its geological implications. Mineral Deposits 31 (5), 1119–1131 (in Chinese with English abstract).
Guo, X.J., Li, Y., Kong, L.H., Zheng, J.H., Sun, D.Q., 2015. Geological characteristics and metallogenesis of the Boketubayi iron–manganese deposit in Altay, Xinjiang. Geoscience 29 (6), 1309–1318 (in Chinese with English abstract).
Guy, A., Schulmann, K., Munschy, M., Miehe, J.-M., Edel, J.B., Lexa, O., Fairhead, D., 2014. Geophysical constraints for terrane boundaries in southern Mongolia. J. Geophys. Res. Solid Earth 119 (10), 7966–7991.
Han, B., Ji, J., Song, B., Chen, L., Li, Z., 2004. SHIMP zircon U–Pb age of Kalatongke no. 1 and Huangshandong Cu–Ni-bearing mafic-ultramafic complexes, North Xinjiang, and geological implications. Chin. Sci. Bull. 49, 2424–2429.
Hanžl, P., Schulmann, K., Janousek, V., Lexa, O., Hrdličková, K., Jiang, Y., Buriánek, D., Altanbaatar, B., Ganchuluun, T., Erban, V., 2016. Making continental crust origin of Devonian orthogneisses from SE Mongolian Altai. J. Geosci. 61 (1), 25–50.
He, G., Han, B., Yue, Y., Wang, J., 1990. Tectonic division and crustal evolution of Altay orogenic belt in China. Geosci. Xinjiang 2, 9–20 (in Chinese with the English abstract).

Hermann, J., Rubatto, D., 2003. Relating zircon and monazite domains to garnet growth zones: age and duration of granulite facies metamorphism in the Val Malenco lower crust. J. Metamorph. Geol. 21, 833–852.
Holland, T.J.B., Powell, R., 1998. An internally consistent thermodynamic dataset for phases of petrological interest. J. Metamorph. Geol. 16, 309–344.
Hu, A., Jahn, B.M., Zhang, G., Chen, Y., Zhang, Q., 2000. Crustal evolution and Phanerozoic crustal growth in northern Xinjiang: Nd isotopic evidence – part I. Isotopic characterization of basement rocks. Tectonophysics 328 (1–2), 15–51.
Jahn, B.M., Wu, F., Chen, B., 2000. Granitoids of the Central Asian Orogonic Belt and continental growth in the Phanerozoic. In: Barbarin, B., Stephens, W.E., Bonin, B., Bouchez, J.-L., Clarke, D.B., Cuney, M., Martin, H. (Eds.), The Fourth Hutton Symposium on the Origin of Granites and Realted Rocks. Geological Society of America, Special Papers 350.
Jiang, Y.D., Sun, M., Zhao, G.C., Yuan, C., Xiao, W., Xia, X.P., Long, X.P., Wu, F.Y., 2010. The ~390 Ma high-*T* metamorphic event in the Chinese Altai: a consequence of ridge-subduction? Am. J. Sci. 310 (10), 1421–1452.
Jiang, Y.D., Sun, M., Zhao, G., Yuan, C., Xiao, W.J., 2011. Precambrian detrital zircons in the Early Paleozoic Chinese Altia: their provenance and implications for the crustal growth of central Asia. Precambrian Res. 189, 140–154.
Jiang, Y.D., Štípská, P., Sun, M., Schulmann, K., Zhang, J., Wu, Q.H., Long, X.P., Yuan, C., Racek, M., Zhao, G.C., Xiao, W.J., 2015. Juxtaposition of Barrovian and migmatite domains in the Chinese Altai: a result of crustal thickening followed by doming of partially molten lower crust. J. Metamorph. Geol. 33 (1), 45–70.
Jiang, Y.D., Schulmann, K., Sun, M., Štípská, P., Guy, A., Janoušek, V., Lexa, O., Yuan, C., 2016. Anatexis of accretionary wedge, Pacific-type magmatism, and formation of vertically stratified continental crust in the Altai Orogenic Belt. Tectonics 35, 3095–3118.
Jiang, Y.D., Schulmann, K., Sun, M., Štípská, P., Guy, A., Lexa, O., Janoušek, V., Yuan, C., 2017. Melting of accretionary wedge and building mature continental crust: insights from the magmatic evolution of the Chinese Altai Orogen, Central Asia. Geodynamics Tectonophys. 8 (3), 481–482.
Kovalenko, V.I., Yarmolyuk, V.V., Kovach, V.P., Kotov, A.B., Kozakov, I.K., Salnikova, E.B., Larin, A.M., 2004. Isotope provinces, mechanisms of generation and sources of the continental crust in the Central Asian mobile belt: geological and isotopic evidence. J. Asia Earth Sci. 23 (5), 605–627.
Kozakov, I., Glebovitsky, V.A., Bibikova, E.V., Azimov, P.Y., Kirnozova, T.I., 2002. Hercynian granulites of Mongolian and Gobian Altai: geodynamic setting and formation conditions. Dokl. Earth Sci. 38, 781–785.
Kröner, A., Lehmann, J., Schulmann, K., Demoux, A., Lexa, O., Tomurhuu, D., Štípská, P., Liu, D., Wingate, M.T.D., 2010. Lithostratigraphic and geochronological constraints on the evolution of the Central Asian Orogenic Belt in SW Mongolia: early Paleozoic rifting followed by late Paleozoic accretion. Am. J. Sci. 310, 523–574.
Lardeaux, J.M., Spalla, M.I., 1991. From granulites to eclogites in the Sesia zone (Italian Western Alps): A record of the opening and closure of the Piedmont ocean. J. Metamorph. Geol. 9 (1), 35–59.
Lehmann, J., Schulmann, K., Lexa, O., Corsini, M., Kröner, A., Štípská, P., Tomurhuu, D., Otgonbator, D., 2010. Structural constraints on the evolution of the Central Asian Orogenic Belt in SW Mongolia. Am. J. Sci. 310 (7), 575–628.
Lehmann, J., Schulmann, K., Lexa, O., Závada, P., Štípská, P., Hasalová, P., Belyanin, G., Corsini, M., 2017. Detachment folding of partiallly molten crust in accretionary orogens: a new magma-enhanced vertical mass and heat transfer mechanism. Lithosphere 9 (6). https://doi.org/10.1130/L670.
Li, X.H., Liu, D.Y., Sun, M., Li, W.X., Liang, X.R., Liu, Y., 2004. Precise Sm–Nd and U–Pb isotopic dating of the supergiant Shizhuyuan polymetallic deposit and its host granite, SE China. Geol. Mag. 141 (2), 225–231.
Li, Z., Li, Y., Chen, H., Santosh, M., Xiao, W., Wang, H., 2010. SHRIMP U–Pb zircon chronology of ultrahigh–temperature spinel–orthopyroxene–garnet granulite from South Altay orogenic belt, northwestern China. Island Arc 19 (3), 506–516.
Li, Z., Yang, X., Li, Y., Santosh, M., Chen, H., Xiao, W., 2014. Late Palaeozoic tectono–metamorphic evolution of the Altai segment of the Central Asian Orogenic Belt: constraints from metamorphic *P–T* pseudosection and zircon U–Pb dating of ultrahigh-temperature granulite. Lithos 204, 83–96.
Li, P., Sun, M., Rosenbaum, G., Cai, K., Yu, Y., 2015a. Structural evolution of the Irtysh Shear Zone (northwestern China) and implications for the amalgamation of arc systems in the Central Asian Orogenic Belt. J. Struct. Geol. 80, 142–156.
Li, P., Yuan, C., Sun, M., Long, X., Cai, K., 2015b. Thermochronological constraints on the late Palaeozoic tectonic evolution of the southern Chinese Altai. J. Asian Earth Sci. 113, 51–60.
Li, P., Sun, M., Rosenbaum, G., Cai, K., Chen, M., He, Y., 2016. Transpressional deformation, strain partitioning and fold superimposition in the southern Chinese Altai, Central Asian Orogenic Belt. J. Struct. Geol. 87, 64–80.
Liu, W., Liu, L.J., Liu, X.J., Shang, H.J., Zhou, G., 2010. Age of the Early Devonian Kangbutiebao Formation along the southern Altay Mountains and its northeastern extension. Acta Petrol. Sin. 26 (2), 387–400 (in Chinese with the English abstract).
Long, X., Sun, M., Yuan, C., Xiao, W., Lin, S., Wu, F., Cai, K., 2007. Detrital zircon age and Hf isotopic studies for metasedimentary rocks from the Chinese Altai: implications for the Early Paleozoic tectonic evolution of the Central Asian Orogenic Belt. Tectonics 26 (5), 1–20.
Long, X., Sun, M., Yuan, C., Xiao, W., Cai, K., 2008. Early Paleozoic sedimentary record of the Chinese Altai: implications for its tectonic evolution. Sediment. Geol. 208, 88–100.
Long, X., Yuan, C., Sun, M., Xiao, W., Zhao, G., Wang, J., Cai, K., Xia, X., Xie, L., 2010. Detrital zircon ages and Hf isotopes of the early Paleozoic flysch sequence in the Chinese Altai, NW China: new constrains on depositional age, provenance and tectonic evolution. Tectonophysics 480 (1–4), 213–231.
Long, X., Yuan, C., Sun, M., Safonova, I., Xiao, W., Wang, Y., 2012. Geochemistry and U – Pb detrital zircon dating of Paleozoic greywackes in East Junggar, NW China: insight into subduction-accretion process in the southern Central Asian Orogenic Belt. Gondwana Res. 21, 637–653.
Lv, Z.-H., Zhang, H., Tang, Y., Guan, S.J., 2012. Petrogenesis and magmatic hydrothermal evolution time limitation of Kelumute No. 112 pegmatite in Altay, Northwestern China: evidence from zircon U–Pb and Hf isotopes. Lithos 154, 374–391.
Ma, Z.-L., 2014. Zircon U–Pb dating and Hf Isotopes of Pegmatites from the Kaluan Mining Area in the Altay, Xinjiang and Their Genetic Relationship With the Halong Granite. A dissertation submitted to graduate university of Chinese Academy of Sciences for the degree of Master of Philosophy. pp. 1–70 (in Chinese with English abstract).
Martelat, J.E., Lardeaux, J.M., Nicollet, C., Rakotondrazafy, R., 2000. Strain pattern and late Precambrian deformation history in southern Madasgascar. Precambrian Res. 102 (1–2), 1–20.
Mossakovsky, A.A., Ruzhentsev, S.V., Samygin, S.G., Kheraskova, T.N., 1993. The central Asian fold belt: geodynamic evolution and formation history. Geotectonics 26, 455–473.
Nakano, N., Osanai, Y., Owada, M., Satish-Kumar, M., Adachi, T., Jargalan, S., Yoshimoto, A., Syeryekhan, K., Boldbaatar, C.H., 2015. Multiplegrowth of garnet, sillimanite/kyanite and monazite during amphibolite-facies metamorphism: implications for the *P–T–t* and tectonic evolution of the western Altai range, Mongolia. J. Metamorph. Geol. 33 (9), 937–958.
Pirajno, F., Mao, J., Zhang, Z., Zhang, Z., Chai, F., 2008. The association of mafic–ultramafic intrusions and A-type magmatism in the tian Shan and Altay orogens, NW China: implications for geodynamic evolution and potential for the discovery of new ore deposits. J. Asian Earth Sci. 32, 165–183.
Ren, B.Q., Zhang, H., Tang, Y., Lv, Z.H., 2011. LA-ICP-MS U–Pb zircon geochronology of the Altai pegmatites and its geological significance. Acta Mineral. Sin. 31 (3), 587–596 (in Chinese with the English abstract).
Rudnick, R.L., Fountain, D.M., 1995. Nature and composition of the continental–crust: a lower crustal perspective. Rev. Geoph. 33 (3), 267–309.
Schulmann, K., Kröner, A., Hegner, E., Wendt, I., Konopasek, J., Lexa, O., Štípská, P., 2005. Chronological constraints on the pre-orogenic history, burial and exhumation of deep-seated rocks along the eastern margin of the Varsican Orogen, Bohemia Massi, Czech Republic. Am. J. Sci. 305 (5), 407–448.
Sengör, A.M.C., Natal'In, B.A., Burtman, V.S., 1993. Evolution of the Altaid tectonic collage and Palaeozoic crustal growth in Eurasia. Nature 364, 299–307.
Shan, Q., Zeng, Q.S., Luo, Y., Yang, W.B., Zhang, H., Qiu, Y.Z., Yu, X.Y., 2011. SHRIMP U–Pb ages and petrology studies on the potassic and sodic rhyolites in Altai, North Xinjiang. Acta Petrol. Sin. 27 (12), 3653–3665 (in Chinese with English abstract).
Sun, M., Yuan, C., Xiao, W., Long, X., Xia, X., Zhao, G., Lin, S., Wu, F., Kröner, A., 2008. Zircon U–Pb and Hf isotopic study of gneissic rocks from the Chinese Altai: progressive accretionary history in the Early to Middle Palaeozoic. Chem. Geol. 247 (3), 352–383.
Sun, M., Long, X., Cai, K., Jiang, Y., Wang, B., Yuan, C., Zhao, G., Xiao, W., Wu, F., 2009. Early Palaeozoic ridge subduction in the Chinese Altai: insight from the abrupt change in zircon Hf isotopic compositions. Sci. China Ser. D Earth Sci. 52 (9), 1345–1358.
The Team One of Geological Survey of Xinjiang, 1979. Four Unpublished Geological Maps of Altai, With Geological Report, scale 1/200,000.
Tong, Y., Wang, T., Hong, D., Han, B., 2006. Pb isotopic compositions of granitoids from the Altay Orogen (China): evidence for mantle-derived origin and continental growth. Acta Geol. Sin. 40, 517–528 (in Chinese with English abstract).
Tong, Y., Wang, T., Hong, D., Dai, Y.J., Han, B.F., Liu, X.M., 2007. Age and origin of the early Devonian granites from the north part of the Chinese Altai Moutains and its tectonic implications. Acta Geol. Sin. 23 (8), 1933–1944.
Tong, L., Chen, Y., Xu, Y., Zhou, X., Liu, Z., 2013. Zircon U–Pb ages of the ultrahigh-temperature metapelitic granulite from the Altai orogeny, NW China, and geological implications. Acta Petrol. Sin. 29, 3435–3445 (in Chinese with the English abstract).
Tong, L., Xu, Y.-G., Cawood, P.A., Zhou, X., Chen, Y., Liu, Z., 2014a. Anticlockwise *P–T* evolution at ~280 ma recorded from ultrahigh-temperature metapelitic granulite in the Chinese Altai orogenic belt, a possible link with the Tarim mantle plume? J. Asian Earth Sci. 94 (0), 1–11.
Tong, Y., Wang, T., Jahn, B.M., Sun, M., Hong, D.W., Gao, J.F., 2014b. Post-accretionary Permian granitoids in the Chinese Altai orogen: geochronology, petrogenesis and tectonic implications. Am. J. Sci. 314 (1), 80–109.
Vermeesch, P., 2012. On the visualisation of detrital age distributions. Chem. Geol. 312-313, 190–194.
Wan, B., Xiao, W., Zhang, L., Windley, B.F., Han, C., Quinn, C.D., 2011. Contrasting styles of mineralization in the Chinese Altai and east Junggar, NW China: implications for the accretionary history of the southern Altaids. J. Geol. Soc. Lond. 168, 1311–1321.
Wan, B., Xiao, W., Windley, B.F., Yuan, C., 2013. Permian hornblende gabbros in the Chinese Altai from a subduction-related hydrous parent magma, not from the Tarim mantle plume. Lithosphere 5, 290–299.
Wang, Y., Mooney, W.D., Yuan, X., Coleman, R.G., 2003. The crustal structure from the Altai Mountains to the Altyn Tagh fault, Northwest China. J. Geophys. Res. Solid Earth 108.
Wang, T., Hong, D.W., Jahn, B.M., Tong, Y., Wang, Y.B., Han, B.F., Wang, X.X., 2006. Timing, petrogenesis, and setting of Palaeozoic synorogenic intrusions from the Altai Mountains, Northwest China: implications for the tectonic evolution of an accretionary orogen. J. Geol. 114 (6), 735–751.
Wang, T., Tong, Y., Jahn, B.M., Zou, T.R., Wang, Y.B., Hong, D.W., Han, B.F., 2007. SHRIMP zircon U–Pb geochronology of no. 3 pegmatite from the Altai orogen, NW China, and its implications. Ore Geol. Rev. 32, 325–336.
Wang, T., Jahn, B.M., Kovach, V.P., Tong, Y., Hong, D.W., Han, B.F., 2009a. Nd–Sr isotopic mapping of the Chinese Altai and implications for continental growth in the central Asian Orogenic Belt. Lithos 110 (1), 359–372.
Wang, W., Wei, C., Wang, T., Lou, Y., Chu, H., 2009b. Confirmation of pelitic granulite in the Altai orogen and its geological significance. Chin. Sci. Bull. 54 (14), 2543–2548.

Wang, W., Wei, C., Zhang, Y., Chu, H., Zhao, Y., Liu, X., 2014a. Age and origin of sillimanite schist from the Chinese Altai metamorphic belt: implications for late Palaeozoic tectonic evolution of the central Asian Orogenic Belt. Int. Geol. Rev. 56 (2), 224–236.

Wang, Y., Long, X., Wilde, S.A., Xu, H., Sun, M., Xiao, W., Yuan, C., Cai, K., 2014b. Provenance of Early Palaeozoic metasediments in the central Chinese Altai: implications for tectonic affinity of the Altai-Mongolia terrane in the Central Asian Orogenic Belt. Lithos 210–211 (0), 57–68.

Wei, C., Clarke, G., Tian, W., Qiu, L., 2007. Transition of metamorphic series from the Kyanite-to andalusite-types in the Altai orogen, Xinjiang, China: evidence from petrography and calculated KMnFMASH and KFMASH phase relations. Lithos 96 (3), 353–374.

Windley, B.F., Kröner, A., Guo, J., Qu, G., Li, Y., Zhang, C., 2002. Neoproterozoic to Palaeozoic geology of the Altai Orogen, NW China: new zircon age data and tectonic evolution. The Journal of Geology 110, 719–737.

Windley, B.F., Alexeiev, D., Xiao, W.J., Kröner, A., Badarch, G., 2007. Tectonic models for accretion of the Central Asian Orogenic Belt. J. Geol. Soc. Lond. 164, 31–47.

Xiao, X.C., Tang, Y.Q., Feng, Y.M., Zhu, B.Q., Li, J.Y., Zhao, M., 1992. Tectonic Evolution of the Northern Xinjiang and its Adjacent Region. Geological Publishing House, Beijing, pp. 1–180 (in Chinese with English abstract).

Xiao, W.J., Zhang, L.C., Qin, K.Z., Sun, S., Li, J.L., 2004. Palaeozoic accretionary and collisional tectonics of the Eastern Tianshan (China): implications for the continental growth of central Asia. Am. J. Sci. 304 (5), 370–395.

Xiao, W.J., Windley, B.F., Sun, S., Li, J.L., Huang, B.C., Han, C.M., Yuan, C., Sun, M., Chen, H.L., 2015. A tale of amalgamation of three Permo-Triassic collage systems in Central Asia: Oroclines, sutures, and terminal accretion. Annu. Rev. Earth Planet. Sci. 43, 477–507.

Xiao, W.J., Windley, B.F., Han, C.M., Liu, W., Wan, B., Zhang, J.E., Ao, S.J., Zhang, Z.Y., Song, D. F., 2018. Late Paleozoic to early Triassic multiple roll-back and oroclinal bending of the Mongolia collage in Central Asia. Earth Sci. Rev. https://doi.org/10.1016/j.earscirev.2017.09.020 (in press).

Yang, T.N., Li, J.Y., Zhang, J.E., Hou, K.J., 2011. The Altai-Mongolia terrane in the central Asian Orogenic Belt (CAOB): a peri-Gondwana one? Evidence from zircon U–Pb, Hf isotopes and REE abundance. Precambrian Res. 187 (1), 79–98.

Yang, C., Yang, F., Chai, F., Wu, Y., 2018. Timing of formation of the Keketale Pb–Zn deposit, Xinjiang, Northwest China, central Asian Orogenic Belt: implications for the metallogeny of the South Altay Orogenic Belt. Geol. J. 53, 899–913.

Yarmolyuk, V.V., Kuzmin, M.I., Kozlovsky, A.M., 2013. Late paleozoic-Early Mesozoic within-plate magmatism in North Asia: traps, rifts, giant batholiths, and the geodynamics of their origin. Petrology 21 (2), 101–126.

Yuan, C., Sun, M., Xiao, W., Li, X., Chen, H., Lin, S., Xia, X., Long, X., 2007. Accretionary orogenesis of the Chinese Altai: insights from Paleozoic granitoids. Chem. Geol. 242 (1), 22–39.

Zhang, J., Wang, J., Ding, R., 2000. Characteristics and U–Pb ages of zircon in metavolcanics from the Kangbutiebao Formation in the Altay orogen, Xinjiang. Reg. Geol. China 19 (3), 281–287 (in Chinese with English abstract).

Zhang, C.L., Li, Z.X., Li, X.H., Xu, Y.G., Zhou, G., Ye, H.M., 2010. A Permian large igneous province in Tarim and central Asian Orogenic Belt (CAOB), NW China: results of a ca. 275 ma mantle plume? Geol. Soc. Am. Bull. 122, 2020–2040.

Zhang, C.L., Santosh, M., Zou, H.B., Xu, Y.G., Zhou, G., Dong, Y.G., Wang, H.Y., 2012. Revisiting the "Irtish tectonic belt": implications for the Palaeozoic tectonic evolution of the Altai orogen. J. Asian Earth Sci. 52, 117–133.

Zhang, C.L., Zou, H.B., Yao, C.Y., Dong, Y.G., 2014. Origin of Permian gabbroic intrusions in the southern margin of the Altai orogenic belt: a possible link to the Permian Tarim mantle plume? Lithos 204, 112–124.

Zhang, J., Sun, M., Schulmann, K., Zhao, G., Wu, Q., Jiang, J.D., Guy, A., Wang, Y., 2015. Distinct deformational history of two contrasting tectonic domains in the Chinese Altai: their significance in understanding accretionary orogenic process. J. Struct. Geol. 73, 64–82.

Zhang, X., Zhang, H., Ma, Z.-L., Tang, Y., Lv, Z.-H., Zhao, J.-Y., Liu, Y.-L., 2016. A new model for the granite–pegmatite genetic relationships in the Kaluan–Azubai–Qiongkuer pegmatite-related ore fields, the Chinese Altay. J. Asian Earth Sci. 124, 139–155.

Zheng, C.Q., Kato, T., Enami, M., Xu, X.C., 2007. CHIME monazite ages of metasediments from the Altai orogen in northwestern China: Devonian and Permian ages of metamorphism and their significance. Island Arc 16 (4), 598–604.

Zhuang, Y., 1994. The PTst evolution of metamorphism and development mechanism of the thermal - structural - gneiss domes in the Chinese Altaides. Acta Geol. Sin. 7 (3), 267–281.